The Astrophysical Journal, 854:151 (20pp), 2018 February 20 https://doi.org/10.3847/1538-4357/aaabb7

The Strong Gravitationally Lensed *Herschel* Galaxy HLock01: Optical Spectroscopy Reveals a Close Galaxy Merger with Evidence of Inflowing Gas

Rui Marques-Chaves[1,2], Ismael Pérez-Fournon[1,2], Raphael Gavazzi[3], Paloma I. Martínez-Navajas[1,2], Dominik Riechers[4], Dimitra Rigopoulou[5], Antonio Cabrera-Lavers[1,6], David L. Clements[7], Asantha Cooray[8], Duncan Farrah[9], Rob J. Ivison[10,11], Camilo E. Jiménez-Ángel[1,2], Hooshang Nayyeri[8], Seb Oliver[12], Alain Omont[3], Douglas Scott[13], Yiping Shu[14,15], and Julie Wardlow[16]

[1] Instituto de Astrofísica de Canarias, C/Vía Láctea, s/n, E-38205 San Cristóbal de La Laguna, Tenerife, Spain
[2] Universidad de La Laguna, Dpto. Astrofísica, E-38206 San Cristóbal de La Laguna, Tenerife, Spain
[3] Institut d'Astrophysique de Paris, UMR7095 CNRS & Sorbonne Université (UPMC), F-75014 Paris, France
[4] Astronomy Department, Cornell University, Ithaca, NY 14853, USA
[5] Astrophysics, Department of Physics, University of Oxford, Keble Road, Oxford, OX1 3RH, UK
[6] GRANTECAN, Cuesta de San José s/n, E-38712, Breña Baja, La Palma, Spain
[7] Astrophysics Group, Imperial College London, Blackett Laboratory, Prince Consort Road, London SW7 2AZ, UK
[8] Department of Physics and Astronomy, University of California, Irvine, CA 92697, USA
[9] Department of Physics, Virginia Tech, Blacksburg, VA 24061, USA
[10] European Southern Observatory, Karl-Schwarzschild-Str. 2, D-85748 Garching, Germany
[11] Institute for Astronomy, University of Edinburgh, Royal Observatory, Blackford Hill, Edinburgh EH9 3HJ, UK
[12] Astronomy Centre, Department of Physics and Astronomy, University of Sussex, Brighton BN1 9QH, UK
[13] Department of Physics and Astronomy, University of British Columbia, 6224 Agricultural Road, Vancouver, BC V6T 1Z1, Canada
[14] National Astronomical Observatories, Chinese Academy of Sciences, A20 Datun Road, Chaoyang District, Beijing 100012, People's Republic of China
[15] Purple Mountain Observatory, Chinese Academy of Sciences, 2 West Beijing Road, Nanjing 210008, People's Republic of China
[16] Centre for Extragalactic Astronomy, Department of Physics, Durham University, South Road, Durham DH1 3LE, UK
Received 2017 December 18; revised 2018 January 25; accepted 2018 January 28; published 2018 February 21

Abstract

The submillimeter galaxy (SMG) HERMES J105751.1+573027 (hereafter HLock01) at $z = 2.9574 \pm 0.0001$ is one of the brightest gravitationally lensed sources discovered in the *Herschel* Multi-tiered Extragalactic Survey. Apart from the high flux densities in the far-infrared, it is also extremely bright in the rest-frame ultraviolet (UV), with a total apparent magnitude $m_{\rm UV} \simeq 19.7$ mag. We report here deep spectroscopic observations with the Gran Telescopio Canarias of the optically bright lensed images of HLock01. Our results suggest that HLock01 is a merger system composed of the *Herschel*-selected SMG and an optically bright Lyman break-like galaxy (LBG), separated by only 3.3 kpc in projection. While the SMG appears very massive ($M_* \simeq 5 \times 10^{11}\,M_\odot$), with a highly extinguished stellar component ($A_V \simeq 4.3$), the LBG is a young, lower-mass ($M_* \simeq 1 \times 10^{10}\,M_\odot$), but still luminous ($10 \times L^*_{\rm UV}$) satellite galaxy. Detailed analysis of the high signal-to-noise ratio (S/N) rest-frame UV spectrum of the LBG shows complex kinematics of the gas, exhibiting both blueshifted and redshifted absorption components. While the blueshifted component is associated with strong galactic outflows from the massive stars in the LBG, as is common in most star-forming galaxies, the redshifted component may be associated with gas inflow seen along a favorable sightline to the LBG. We also find evidence of an extended gas reservoir around HLock01 at an impact parameter of 110 kpc, through the detection of C II $\lambda\lambda$1334 absorption in the red wing of a bright Lyα emitter at $z \simeq 3.327$. The data presented here highlight the power of gravitational lensing in high S/N studies to probe deeply into the physics of high-z star-forming galaxies.

Key words: cosmology: observations – galaxies: evolution – galaxies: individual (HLock01) – galaxies: starburst – gravitational lensing: strong

1. Introduction

High-z submillimeter galaxies (SMGs) represent a population of the most massive and luminous galaxies in the early universe. They are characterized by dust-enshrouded vigorous star formation, assembling their mass very rapidly over short timescales, the so-called starburst phase (see Blain et al. 2002; Casey et al. 2014, for reviews). They are believed to be the progenitors of massive elliptical galaxies predominantly found in clusters of galaxies at lower redshifts (e.g., Daddi et al. 2009; Capak et al. 2011; Walter et al. 2012; Dannerbauer et al. 2014; Riechers et al. 2014; Casey et al. 2015; Oteo et al. 2017b), and the study of this population is vital to understand their formation and subsequent evolution.

Despite the huge progress made over the past decades in understanding the properties of SMGs (e.g., Greve et al. 2005; Magnelli et al. 2012; Riechers et al. 2013; Dowell et al. 2014; Ivison et al. 2016; Michałowski et al. 2017; Oteo et al. 2017a), the main mechanism that drives the intense star formation responsible for the high far-IR luminosities is still a matter of debate (e.g., Swinbank et al. 2008; González et al. 2011; Michałowski et al. 2012; Hayward et al. 2013; Narayanan et al. 2015). On one hand, almost all ultraluminous galaxies in the local universe are interacting galaxies and mergers (e.g., Farrah et al. 2001, 2002; Bridge et al. 2007; Haan et al. 2011). At high-z, a considerable number of SMGs are also found to be galaxy mergers (e.g., Capak et al. 2008; Ivison et al. 2008, 2013; Tacconi et al. 2008; Fu et al. 2013; Messias et al. 2014; Rawle et al. 2014; Oteo et al. 2016; Riechers et al. 2017; Marrone et al. 2018), although isolated clumpy gas-rich disk galaxies can also reach extremely large SFRs (e.g., Tacconi et al. 2010; Bournaud et al. 2014). On the other hand, some authors suggest, based on simulations, that high star formation

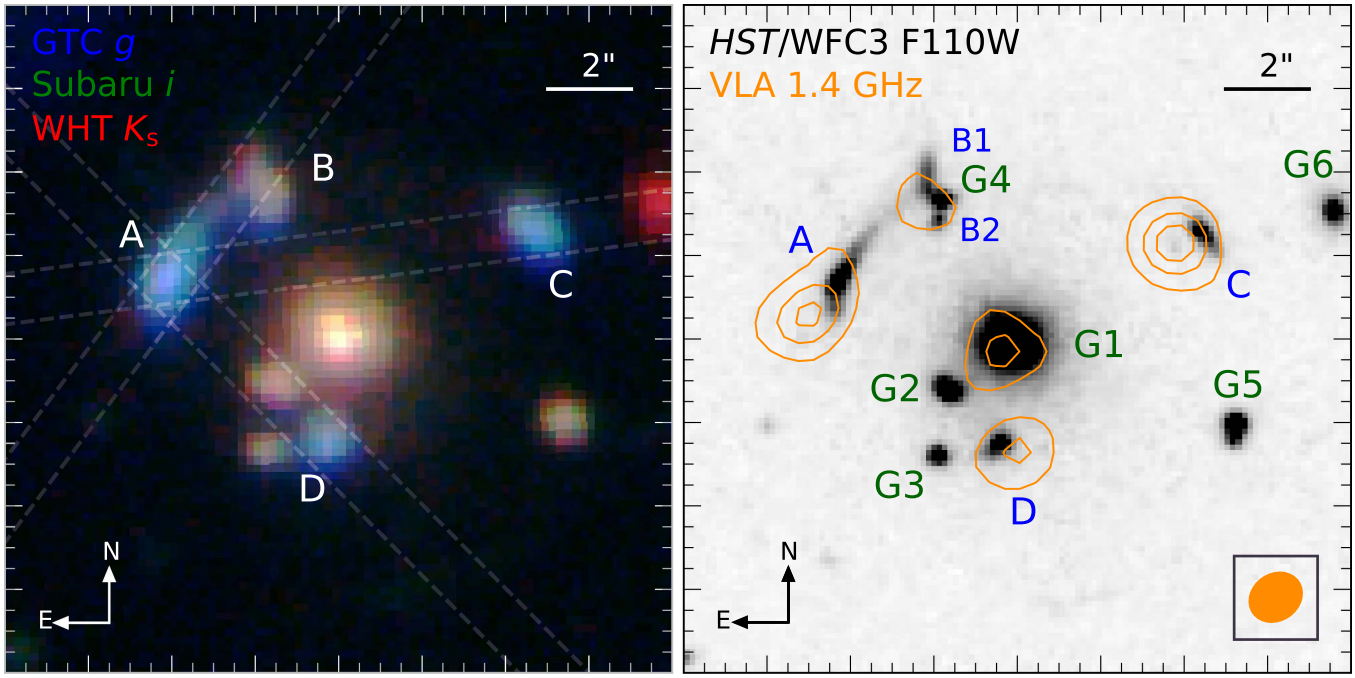

Figure 1. Left panel: g, I, and K_s color image of HLock01 from GTC, Subaru, and WHT, respectively. Dashed lines show the positions of OSIRIS long-slit spectroscopic observations, all centered on the brightest lensed image A, and oriented so as to encompass the other bright lensed images B–D. Right panel: near-IR high-resolution *HST*/WFC3 F110W image with labeled multiply lensed images at $z \simeq 2.95$ (blue) and foreground galaxies at $z \simeq 0.65$ (green). G4 is massive enough to split the lensed image B into two pieces on both sides (B1 and B2, see more details in Gavazzi et al. 2011). Orange contours show VLA data at 1.4 GHz, and its beam is shown on the bottom right. A spatial offset of the bright lensed images is seen between the short (*HST* F110W, HLock01-B) and long wavelengths (VLA, HLock01-R). Each image is $16'' \times 16''$, centered on the brightest lensing galaxy, G1, and oriented such that north is up and east is to the left.

rates (SFRs $\gtrapprox$ 1000 $M_\odot$ yr^{-1}) in some SMGs are difficult to explain by a merger scenario alone, and propose that the predominant mechanism is smooth accretion of cold gas or infall of gas previously ejected via stellar feedback (e.g., Kereš et al. 2005; Dekel et al. 2009; Narayanan et al. 2015).

Whatever the mechanisms responsible for such extremely large SFRs are, this active phase of SMGs is a clear indication of intense ionizing flux from a young, massive stellar population that dominates the rest-frame ultraviolet (UV). It is thus important to provide detailed characterization of the physical properties of the early episodes of star formation in these galaxies, via spectral diagnostics in the rest-frame UV. However, such studies are limited by the faintness of these galaxies at short wavelengths, with the massive stars giving rise to the UV continuum being embedded in large quantities of dust. Considerable spectroscopic efforts have been successfully used to obtain accurate spectroscopic redshifts, probe for signs of active galactic nucleus (AGN) activity, and investigate properties of the ionized gas in SMGs, mainly by using rest-frame optical nebular emission lines (e.g., Chapman et al. 2004, 2005; Swinbank et al. 2004, 2005, 2006; Alaghband-Zadeh et al. 2012; Olivares et al. 2016; Casey et al. 2017; Danielson et al. 2017). However, the typical faintness of high-z galaxies and the dust obscuration of SMGs make it almost impossible with current facilities to obtain high signal-to-noise ratio (S/N) spectra, a requirement for properly studying the properties of the young stars, and to look for signatures of outflowing/inflowing gas.

One exception to this principle is the galaxy discussed in this paper, the strong gravitationally lensed SMG HERMES J105751.1+573027 (hereafter HLock01), which is unusually bright in both the optical ($R \simeq 19.7$ mag) and in the far-IR ($S_{250\,\mu m} \simeq 400$ mJy). HLock01 was identified with *Herschel*/SPIRE in the *Herschel* Multi-tiered Extragalactic Survey (HerMES; Oliver et al. 2012), and investigated in a series of papers after significant follow-up effort (Conley et al. 2011; Gavazzi et al. 2011; Riechers et al. 2011; Scott et al. 2011; Bussmann et al. 2013; Wardlow et al. 2013). Here we give a summary of the main results from those papers. The discovery and its lensing nature were first presented by Conley et al. (2011), based on 880 μm Submillimeter Array (SMA) interferometry and near-IR K_p adaptive optics (AO) observations using NIRC2 on the Keck-II telescope, in which the *Herschel* source was resolved into four components with a large separation of around 9″ (see Figure 1). Using the Plateau de Bure Interferometer (PdBI), the Combined Array for Research in Millimeter-wave Astronomy (CARMA), and the Green Bank Telescope (GBT), Riechers et al. (2011) and Scott et al. (2011) established the redshift of HLock01 from several CO molecular emission lines as $z_{CO} = 2.9574 \pm 0.0001$. By studying the kinematics of the gas reservoir, Riechers et al. (2011) found a resolved velocity structure in the CO ($J = 5 \rightarrow 4$) emission, similar to what is observed in gas-rich mergers, but the low spatial resolution did not allow a definitive conclusion. The lens modeling was performed by Gavazzi et al. (2011) using NIRC2 K_p and IRAM CO ($J = 5 \rightarrow 4$) imaging, as well as deep optical I band imaging with the Subaru Telescope. They showed that the rest-frame UV and optical emission is magnified by a factor of $\mu = 10.9 \pm 0.7$ by a small group of galaxies at $z_{phot} \simeq 0.6$. However, an offset of 2.4 kpc in the source plane was found between the stars that emit at visible/near-IR wavelengths and the gas distribution traced by the molecular gas.

Later on, Bussmann et al. (2013) and Wardlow et al. (2013) presented new imaging data for this system, using *Hubble Space Telescope* (*HST*) WFC3 F110W, new 880 μm SMA with higher spatial resolution than the data presented in Conley et al.

Table 1
OSIRIS Spectroscopic Observations of HLock01-B

Lensed Images	PA (°)	Grism	Date	Time (s)	Seeing (arcsec)	Moon
A/B	−39.5	R2500V	2015 May 09	5 × 900	0.7	dark
	−39.5	R2500R	2015 May 09	5 × 900	0.8	dark
A/C	−82.2	R2500V	2015 May 08	3 × 900	1.0	gray
	−82.2	R2500V	2015 Jun 07	2 × 900	0.9	gray
	−82.2	R2500R	2015 Apr 26	3 × 900	0.8	gray
	−82.2	R2500R	2015 Jun 07	2 × 900	0.9	gray
A/D	44.0	R2500V	2015 May 09	3 × 900	0.8	gray
	44.0	R2500V	2015 Jun 11	2 × 900	0.8	dark
	44.0	R2500R	2015 Apr 26	3 × 900	0.7	gray
	44.0	R2500R	2015 Jun 11	2 × 900	0.8	dark

(2011), and Very Large Array (VLA) 1.4 GHz data (at 1.″1 resolution). The new images show the same spatial offsets of the bright lensed images seen between the short and long wavelengths (see Figure 1), noticed by Conley et al. (2011) and Gavazzi et al. (2011). A new lens model was determined by Bussmann et al. (2013) using the SMA 880 μm data, showing a large dust distribution, magnified by 9.2 ± 0.4 with an effective radius of 4 kpc in the source plane. Its centroid matches the position of the gas distribution traced by the molecular gas, which we attribute to the source of the luminous far-IR emission, but both are offset with respect to the stars that are seen in the visible/near-IR (UV/optical in the rest-frame). Finally, Rigopoulou et al. (2018) discuss the applicability of the [O III]88/[N II]122 line ratio as a metallicity indicator in high-redshift submillimeter luminous galaxies and found that the gas metallicity of HLock01 is $0.6 < Z_{\rm gas}/Z_{\odot} < 1.0$.

Due to the high dust content of HLock01, one could expect that its rest-frame UV and optical light are heavily obscured by dust, as in most SMGs. However, HLock01 is unusually bright in its rest-frame UV, and their colors are also consistent with those of $z \sim 3$ Lyman break galaxies (LBGs; Steidel et al. 1996) with $(G–R) = 0.5$ and $(U–G) = 1.4$. In this paper, we present a detailed analysis of the optically bright lensed images of HLock01, based on deep spectroscopic observations with the 10.4 m Gran Telescopio Canarias (GTC). Throughout the paper we adopt the name "HLock01-B" for the optically bright LBG-like galaxy, and "HLock01-R" for the *Herschel*-selected SMG (where "B" and "R" stand for blue and red galaxies, respectively). Thanks to the large collecting area of the GTC, to the lensing magnification of the source, and to the small obscuration toward HLock01-B, we can perform a detailed analysis of its physical properties.

The paper is organized as follows. In Section 2, we describe our spectroscopic and imaging observations. Our analysis of the rest-frame UV spectrum of HLock01-B is presented in Section 3. The main properties of both components of HLock01, derived from SED fitting, are discussed in Section 4. Finally, in Sections 5 and 6, we discus our results and summarize our main findings. A concordance cosmology with matter and dark energy density $\Omega_{\rm m} = 0.3$, $\Omega_{\Lambda} = 0.7$, and Hubble constant $H_0 = 70\,{\rm km\,s^{-1}\,Mpc^{-1}}$ are assumed throughout this work. All magnitudes are given in the AB system.

2. Observations

2.1. GTC/OSIRIS Spectroscopic and Imaging Observations

Rest-frame UV spectroscopic observations were obtained with the Optical System for Imaging and low-Intermediate-Resolution Integrated Spectroscopy instrument (OSIRIS[17]) on the 10.4 m GTC. The data used in this paper were obtained in service mode over seven different nights, between 2015 April 26 and June 21 in dark and gray Moon conditions as part of the GTC program GTCMULTIPLE2A-15A (PI: R. Marques-Chaves). We used the R2500V and R2500R grisms, with dispersions of 0.80 and 1.04 Å $\rm px^{-1}$, respectively. These two grisms provide a full spectral coverage of 4500–7700 Å, which corresponds to 1150–1950 Å in the rest-frame at $z \simeq 2.95$. The OSIRIS 1.″2-wide slit was centered on the brightest lensed image of HLock01-B (image A), and oriented so as to encompass the other lensed images B, C, and D, at sky positions angles (PA) of −39.°4, −82.°9, and 44°, respectively (see Figure 1, left panel). Given this configuration, the corresponding instrumental resolution for the R2500V and R2500R grisms is $\simeq$180 $\rm km\,s^{-1}$. In total, 15 exposures of 900 s were acquired with each grism, equally split between different PAs. A summary of the rest-frame UV spectroscopic observations of HLock01-B used in this work is shown in Table 1.

The data were processed with standard IRAF[18] and PYTHON tasks. Each individual two-dimensional spectrum was bias-subtracted and flat-field corrected. The wavelength calibration was done for every observing night using HgAr+Ne+Xe arc lamps. Finally, individual 2D spectra were background subtracted. The 1D spectra were then extracted and corrected for the instrumental response using observations of the standard stars Ross 640 and GD 153.

We also obtained spectra of the galaxies in the group responsible for the gravitational lensing of HLock01, with two additional long-slit spectra to encompass G1–G4, and G3–G5, respectively. For this, we used a lower spectral resolution grism, R1000R, which provides a wider spectral range (5100–10000 Å), which with a 1.″2-wide slit gives a spectral resolution of $\simeq$400 $\rm km\,s^{-1}$. The other lensing galaxies, G2 and G6, are covered by the long-slit spectra discussed before to study the lensed images of HLock01-B. For the galaxies G1 and G2, we detect several absorption lines (e.g., K and H of Ca II $\lambda\lambda$3934,3969, H_{δ} $\lambda\lambda$4102, and Mgb $\lambda\lambda$5176), as well as a prominent Balmer break at redshift $z_{\rm G1} = 0.6464 \pm 0.0007$, and $z_{\rm G2} = 0.6492 \pm 0.0009$, respectively. The spectra of G3, G4, and G5 are too noisy for a reliable measurement of their redshifts, but we marginally detect a jump at 6500–6600 Å, compatible with a Balmer break at $z \simeq 0.65$. Thus it appears that these galaxies belong to a group at $z \simeq 0.65$, slightly larger

[17] http://www.gtc.iac.es/instruments/osiris/
[18] http://iraf.noao.edu/

than the previously assumed redshift ($z_{\rm phot} = 0.6 \pm 0.04$; Oyaizu et al. 2008). For the brightest member of the group, G1, we measured a large velocity dispersion $\sigma = (438 \pm 30)$ km s^{-1}, in agreement with the velocity dispersion of the deflector found in the lens model presented in Gavazzi et al. (2011), indicating that the background sources are lensed by a galaxy group-scale dark matter halo.

Additionally, broadband imaging with the Sloan g' filter was obtained with OSIRIS on 2017 January 24, as part of the GTC program GTCMULTIPLE3A-16B (PI: I. Pérez-Fournon). The total exposure time was 2160 s, split into 12 individual exposures of 180 s each. Each frame was reduced individually following standard reduction procedures in IRAF. The registration and combination were done using SCAMP (Bertin 2006) and SWARP (Bertin 2010). The seeing of the final image is $\simeq$0.″8 (full width at half maximum, FWHM).

2.2. William Herschel Telescope (WHT)/LIRIS Near-IR Imaging

Near-IR broadband imaging was obtained on 2011 March 22 in the $K_{\rm s}$ filter (PI: I. Pérez-Fournon), using the Long-slit Intermediate Resolution Infrared Spectrograph instrument (LIRIS) mounted at the WHT. LIRIS has a field of view of 4.′27 × 4.′27 with a plate scale of 0.″25 pixel^{-1}. The total integration time was 60 minutes, spit into 180 individual exposures of 20 s, adopting a random dither pattern in 15 different positions. The data reduction was carried out using the IAC's IRAF LIRISDR[19] task. The seeing of the final image was 0.″63 FWHM. The astrometric and flux calibrations were performed using 2MASS stars in the field.

2.3. Ancillary Data

Additional data used in this work consist of a combination of shallow and deep images. Archival U and R wide-field images and catalogs from MEGACAM on the Canada–France–Hawaii Telescope (CFHT), processed and stacked using the MegaPipe image staking pipeline (Gwyn 2008), were downloaded from the Canadian Astronomy Data Centre (CADC[20]). Total exposure times are 4200 and 3300 s in U and R bands, with an average seeing of 0.″83 and 0.″73 FWHM, respectively. HLock01 was also imaged with WFC3 on *HST* under the snapshot program 12488 (PI: Negrello). The source was observed in the broadband filter F110W with a total exposure time of 276.1 s. The *HST* imaging was initially presented in Bussmann et al. (2013) and Wardlow et al. (2013). *Spitzer*/IRAC images and catalogs in the 3.6 and 4.5 μm bands from the *Spitzer* Extragalactic Representative Volume Survey (SERVS; Mauduit et al. 2012) were obtained from the IRSA archive.[21] We also used the IRAC and MIPS imaging from the *Spitzer* Wide-Area InfraRed Extragalactic survey data (SWIRE; Lonsdale et al. 2003).

3. Rest-frame UV Spectrum of HLock01-B

As in other star-forming galaxies, the rest-frame UV spectrum of HLock01-B is characterized by the integrated light from the hot young stellar population with superimposed resonant strong absorption lines produced by the interstellar medium (ISM) and stellar winds. These spectral features can provide detailed information on dynamical, physical, and chemical properties of the atomic and ionized gas in the galaxy, as well as insights on the properties of the young OB stars responsible for the bright continuum (e.g., Pettini et al. 2000, 2002; Shapley et al. 2003; Jones et al. 2012; Steidel et al. 2016; Rigby et al. 2017a, 2017b). Large-scale outflows of interstellar gas, resulting from the kinetic energy deposited by the star formation activity, are a common feature in these galaxies (e.g., Shapley et al. 2003; Steidel et al. 2010).

Despite the differences in the S/N of the spectra of the different lensed images, there are no differences in the profiles of the absorption features and no evidence for velocity offsets between them, as expected. Spectra of the lensed images B and D show redder UV slopes (β), likely due to differential extinction from the proximity of their light path to the foreground galaxies. Thus we will focus our rest-frame UV analysis on the spectrum of the lensed image A, which has higher S/N ($\sim$20–40, depending on the wavelength range) and is less affected by absorption in the ISM of the foreground galaxies.

The rest-frame UV spectrum of the lensed image A of HLock01-B, shown in Figure 2, is remarkably similar to the $z \simeq 3$ LBG composite spectrum (Shapley et al. 2003). It shows a damped Lyα absorption line, and a series of strong absorption lines associated with either stellar winds from massive stars (e.g., C IV $\lambda\lambda$1548,1550) or ISM lines of several species. However, there are significant differences between the expected wavelengths and velocities ($\Delta v \simeq 500$ km s^{-1}) of the ISM in the $z \simeq 3$ template (in orange in Figure 2) and in our spectrum (discussed in Section 3.2).

The OSIRIS spectrum also shows several narrow absorption lines produced by intervening systems at lower redshifts along the line of sight to HLock01-B. We identify at least two intervening metal systems at $z = 1.4583 \pm 0.0008$, and $z = 2.1889 \pm 0.0007$. Some of these absorption lines may contaminate the profiles of lines of HLock01-B, and hence they are taken into account in our analysis (in Section 3.2).

In addition, three strong Lyα lines at $z = 2.72$, 3.15, and 3.27 were serendipitously detected in two of our GTC long-slit spectra (see Appendix A). In particular, the Lyα line at $z = 3.27$ is associated with an Lyα emitting galaxy at 14″ SW from the lensing galaxy G1, and shows an unusual absorption line in its red-emission wing consistent with C II $\lambda\lambda$1334 at the redshift of HLock01-R ($z_{\rm CO} = 2.9574$; Riechers et al. 2011; Scott et al. 2011). We discuss this absorption feature in Section 5.3.

3.1. Systemic Redshift of HLock01-B

Stellar photospheric features are formed in the photospheres of hot stars, and although much weaker than the ISM lines, they can provide a measurement of the systemic redshift of the galaxy. Within the wavelength range covered by our data, we identified several photospheric absorption features (marked with dotted lines in Figure 2), but some of them are blends from multiple transitions. Using the cleanest among these, listed in Table 2, we derive the mean redshift of the stars to be $z_{\rm stars} = 2.9546 \pm 0.0004$.

The nebular C III] $\lambda\lambda$1906,1908 emission is weakly detected (3σ) at $z_{\rm C\,III]} = 2.954 \pm 0.002$, in agreement with $z_{\rm stars}$, but the doublet is not resolved in our spectrum, and the existing data are too noisy for a reliable measurement of this feature. Therefore throughout the paper we adopt the redshift of stellar photospheric lines as the systemic redshift of HLock01-B, $z_{\rm sys} = 2.9546 \pm 0.0004$.

[19] http://www.iac.es/galeria/jap/lirisdr/LIRIS_DATA_REDUCTION.html
[20] http://www.cadc-ccda.hia-iha.nrc-cnrc.gc.ca/en/cfht/
[21] http://irsa.ipac.caltech.edu/data/SPITZER/SERVS/

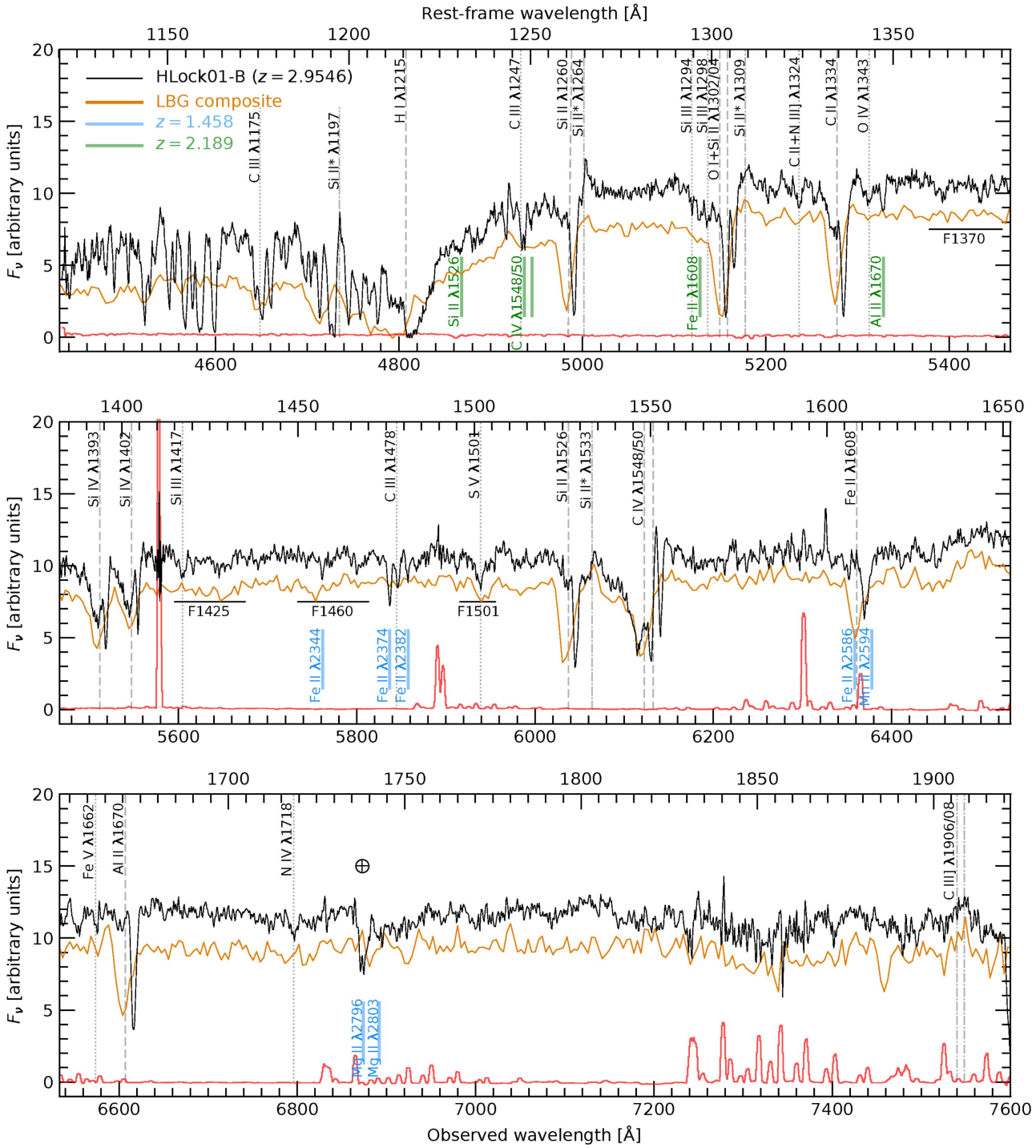

Figure 2. Combined GTC/OSIRIS rest-frame UV spectrum of the lensed image A of HLock01-B. Vertical dotted lines identify the best defined photospheric absorption lines used to derive the systemic redshift of HLock01-B ($z_{\rm sys} = 2.9546 \pm 0.0004$). Strong absorption lines associated with interstellar gas and stellar winds are marked with vertical dashed lines. The C III] λλ1906,1908 nebular emission doublet and fine-structure emission lines of Si II are marked with dash-dotted lines. For comparison, we show in orange the $z \sim 3$ LBG subset composite with the damped Lyα profile from Shapley et al. (2003) at the systemic redshift of HLock01-B (downshifted for clarity). The wavelength windows of four metallicity indices (e.g., F1370, etc.), used to derive the metallicity of young stars in HLock01-B, are also marked. Short vertical blue and green lines mark the positions of absorption lines of intervening systems at $z \simeq 1.458$ and $z \simeq 2.189$, respectively. The sky emission is also plotted in red, showing the locations of strong sky emission lines.

The difference of $\Delta v = 210\,{\rm km\,s^{-1}}$ between the systemic redshift of HLock01-B $z_{\rm sys} = 2.9546$, and the redshift of HLock01-R from the molecular gas lines $z_{\rm CO} = 2.9574$ (Riechers et al. 2011; Scott et al. 2011), cannot be explained by errors in redshift measurements. The velocity offset derived here and the complex dynamical structure of the molecular gas reservoir discussed in Riechers et al. (2011) suggest that HLock01-B is a separate galaxy, different from the *Herschel* SMG (HLock01-R), but both forming a close merger. Nevertheless, similar velocity offsets, interpreted as rotational velocities in some cases, have been found in a few massive galaxies at high-z (e.g., Law et al. 2012; Jiménez-Andrade

Table 2
Stellar Photospheric Lines in HLock01-B

Ion	λ_{lab}[a] (Å)	λ_{obs}[b] (Å)	z_{stars}
Si III	1294.54	5119.71	2.9548 ± 0.0003
C II	1323.93	5235.54[c]	2.9543 ± 0.0006[c]
N III	1324.35	5235.54[c]	2.9543 ± 0.0006[c]
O IV	1343.35	5312.72	2.9546 ± 0.0010
Si III	1417.24	5604.64	2.9546 ± 0.0010
S V	1501.76	5939.25	2.9548 ± 0.0003
N IV	1718.55	6796.37	2.9548 ± 0.0004

Notes.
[a] Vacuum wavelengths.
[b] Values measured from the centroid for the individual photospheric line.
[c] Value refers to the blended C II and N III photospheric lines.

et al. 2017; Toft et al. 2017). A more detailed discussion is presented in Section 5.1.

3.2. Kinematics of the ISM

Within our spectral range, we identify 11 strong absorption features, including low-ionization lines (Si II $\lambda\lambda$1260, O I $\lambda\lambda$1302, Si II $\lambda\lambda$1304, C II $\lambda\lambda$1334, Si II $\lambda\lambda$1526, Fe II $\lambda\lambda$1608, and Al II $\lambda\lambda$1670), and high-ionization lines associated with a hot gas phase (Si IV $\lambda\lambda$ 1393,1402, and C IV $\lambda\lambda$1548,1550). In low-ionization lines, the interstellar component usually dominates over the stellar contribution, and thus they are useful for studying the kinematics of the ISM (Shapley et al. 2003; Steidel et al. 2010). High-ionization lines are associated with strong winds from young stars, and predominantly trace gas at higher temperatures ($T \geqslant 10^4$ K).

For the kinematic analysis of the ISM, we first normalized the GTC/OSIRIS spectrum of HLock01-B using the pseudo-continuum windows that are free of absorption and emission features identified by Rix et al. (2004).

Figure 3 shows the normalized profiles of the strongest absorption lines seen in our spectrum. We note that all ISM lines present an unusual velocity profile with the maximum optical depth located at a mean $v = (+370 \pm 30)$ km s^{-1} relative to the stars of HLock01-B, or $v = (+170 \pm 30)$ km s^{-1} relative to the *Herschel* SMG at $z_{CO} = 2.9574$. This can be understood as gas apparently moving toward the young stars, since all the interstellar lines are seen against the UV stellar continuum. This absorption is strong in the low-ionization lines (the first three columns in Figure 3), likely with saturated profiles,[22] but it is also present, although notably weaker in high-ionization ones, like C IV and Si IV (the last two columns in Figure 3). The spectrum of HLock01-B also shows a secondary but broader absorption component centered at a mean $v = (-220 \pm 60)$ km s^{-1} relative to its systemic redshift, which is a characteristic of large-scale outflows of material in HLock01-B. This blueshifted component is stronger in high-ionization lines than in low-ionization ones (it is detected in C II $\lambda\lambda$1334, Si II $\lambda\lambda$1260, and Si II $\lambda\lambda$1526, but is not clear in O I $\lambda\lambda$1302, Fe II $\lambda\lambda$1608 or Al II$\lambda\lambda$1670), suggesting that the outflowing gas is mostly ionized, or the neutral gas has a lower covering factor than the ionized gas.

The absorption profiles resulting from these two components extend over a velocity range $\Delta v \simeq 1700$ km s^{-1}, from ~ -1000 to $\sim +700$ km s^{-1}, much larger than in other high-z lensed LBGs (Pettini et al. 2000, 2002; Cabanac et al. 2008; Quider et al. 2009, 2010; Dessauges-Zavadsky et al. 2010). The C IV doublet is even broader than the ISM lines, with $\Delta v \gtrsim 3000$ km s^{-1}, indicative of a strong contribution from winds due to radiation pressure of the most massive and luminous stars of HLock01-B. The velocity profile of the C IV doublet shows a strong P-Cygni profile, with the red-emission wing being attenuated by the two narrow, redshifted ($v \simeq +370$ km s^{-1}) interstellar absorption components of C IV.

In order to understand the blueshifed and redshifted ISM absorption components, we simultaneously fit two Gaussians to the low- and high-ionization lines. Figure 4 shows an example of our fit to the low-ionization C II $\lambda\lambda$1334, and high-ionization Si IV $\lambda\lambda$1393 lines, and Table 3 summarizes the results for all strong absorption lines, except the ones that are affected by the proximity of other lines (O I $\lambda\lambda$1302, Si II $\lambda\lambda$1304, and Fe II $\lambda\lambda$1608). In C IV $\lambda\lambda$1548,1550 we only fit the redshifted component, as the blueshifted one is affected by strong winds.

The fitted blueshifted component (blue dashed lines in Figure 4) has its peak located at $z_{blue} = 2.9519 \pm 0.0009$ (or $v_{blue} \simeq -220$ km s^{-1} relative to the systemic redshift of HLock01-B), and shows a broad profile (FWHM $\simeq 900$ km s^{-1}, after accounting for the instrumental broadening) extended over a velocity range from about -1000 to $+600$ km s^{-1}. Despite the fact that a potentially large contribution from stellar winds may be present in the high-ionization lines, for the low-ionization ones, this effect is negligible. Thus the broadness of the blueshifted component in the low-ionization line C II (as well as in others like Si II $\lambda\lambda$1260 and Si II $\lambda\lambda$1526; see Figure 3) suggests highly turbulent kinematics of the outflowing gas. As a comparison, the velocity profile of the low-ionization interstellar lines in the $z \sim 3$ LBGs composite spectrum of Shapley et al. (2003) shows an average FWHM $= (560 \pm 150)$ km s^{-1}. Despite the broadness of the outflowing low-ionization lines in HLock01-B, they show smaller rest-frame equivalent widths (by a factor of two) than in typical LBGs.

The fitted redshifted component (red dashed line in Figure 4) has its peak located at $z_{red} = 2.9596 \pm 0.0003$, and shows a narrow profile (FWHM $= 310$ and 104 km s^{-1}, for C II and Si IV, respectively). If dynamically related to HLock01, its positive velocity relatively to both HLock01-B ($v \simeq +370$ km s^{-1}) and HLock01-R ($v \simeq +170$ km s^{-1}) is indicative of gas moving toward the system. This narrower component is seen in all absorption lines, but appears almost unresolved in the high-ionization ones, suggesting that these lines are dominated by the interstellar component. Moreover, the differences in the FWHM between the redshifted component in low- and high-ionization lines (see Table 3) also suggests that cold and warm gas may have different kinematics and origins. A clearer picture of the origin of this redshifted component of the ISM may come from deeper and higher spectral resolution observations. In particular, fully resolved ISM components of HLock01-B with unsaturated profiles may be used to derive chemical abundances, using the apparent optical depth method, as has been done in other studies of strongly lensed star-forming galaxies (e.g., Pettini et al. 2002; Quider et al. 2009; Dessauges-Zavadsky et al. 2010).

[22] We test if some of these lines are saturated by considering the linear part of the curve of growth. In this case, the ratios of the rest-frame equivalent widths (EW_0) of different transitions of a given ion can be related through their oscillator strengths. For example, for the Si II lines in the unsaturated case, we would expect EW_0 (1260)/EW_0 (1526) $\simeq 5$, EW_0 (1260)/EW_0 (1304) $\simeq 10$, and EW_0 (1304)/EW_0 (1526) $\simeq 0.5$. Our spectrum shows ratios of $\simeq$1.0, 2.5, and 0.4, respectively, suggesting that at least Si II $\lambda\lambda$ 1260 may be saturated.

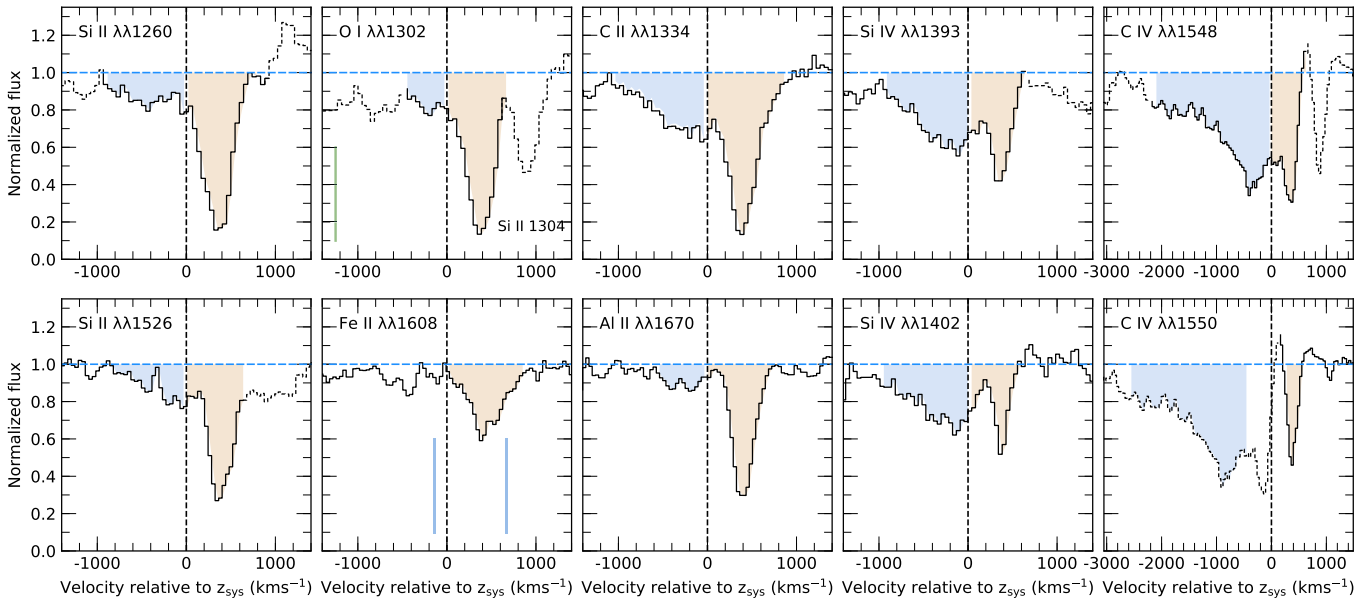

Figure 3. Normalized profiles of low- (first three columns) and high-ionization (last two columns) absorption lines associated with the ISM and stellar winds, respectively. The x axis is the velocity (in km s^{-1}) relative to the stars of HLock01-B, $z_{sys} = 2.9546$, and the y axis is the normalized flux. Almost all ISM and wind lines present an unusual velocity profile, with two distinct absorption components on either side of systemic velocity (negative and positive velocities shaded in blue and red, respectively, for visual purpose only). The absorption component with the maximum intensity is located at $v \simeq +370$ km s^{-1} (shaded in red). Another broader component is also detected in high-ionization lines, like C IV λλ1548,1550 and Si IV λλ1393,1402, and in some ISM lines (shaded in blue). Dotted lines indicate spectral features in HLock01 other than those to which the label in each plot refers. Short vertical blue and green solid lines mark the expected positions of absorption lines from intervening metal systems at lower redshift.

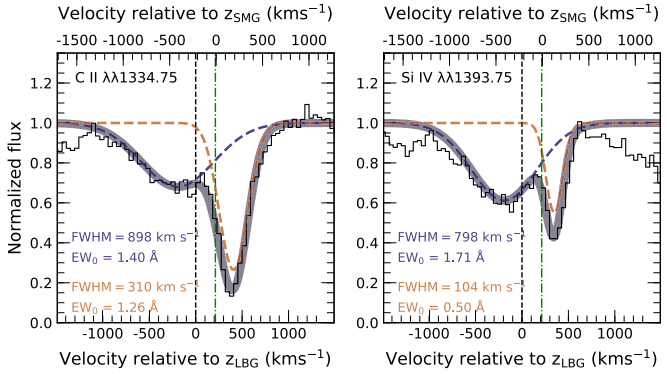

Figure 4. Example of the double-Gaussian fit of the low- (C II λλ1334) and high-ionization lines (Si IV λλ1393). Lower and upper x axes are the velocity (in km s^{-1}) relative to the stars of the LBG (HLock01-B) and to the molecular gas of the SMG (HLock01-R), respectively. The y axis is the normalized flux. The redshifted (red color) and blueshifted (blue color) components represent outflowing and inflowing gas along the line of sight of HLock01-B, respectively. The sum of the two components is also shown in gray. Black dashed and green dotted–dashed vertical lines mark the zero velocity position with respect to $z_{sys} = 2.9546$ (HLock01-B) and $z_{CO} = 2.9574$ (HLock01-R), respectively.

3.3. Stellar Metallicity and Age of HLock01-B

Leitherer et al. (2001), Rix et al. (2004), and later on Sommariva et al. (2012) showed that several blends of stellar UV photospheric absorption lines can be used to trace the metallicity of young stars, by measuring equivalent widths of these blends in specific wavelength windows. These metallicity indicators have been successfully applied in several works (e.g., Quider et al. 2009, 2010; Patrício et al. 2016), using high S/N spectra due to the faintness of these absorption lines. They are defined as the F1370, F1425, F1460, F1501, and F1978 indices, and their wavelength windows are shown in Figure 2 (except for the latter one which is not covered by our data).

We measured the equivalent widths of the features in each of these spectral windows using our normalized spectrum. We then applied the calibrations of Sommariva et al. (2012) to obtain the corresponding metallicity. Table 4 summarizes our measurements. All indices agree in a sub-solar metallicity, and we use the mean value to derive the metallicity of the UV stars in HLock01-B as $Z_{stars} = (0.4 \pm 0.1)Z_{\odot}$.

The strength of any P-Cygni features formed in the expanding winds of the most massive stars is also sensitive to the metallicity, along with the age and the initial mass function (IMF) of the stellar population. In order to study the P-Cygni stellar wind features in HLock01-B, we use model spectra computed with the spectral synthesis code Starburst99 (Leitherer et al. 1999, 2001) and perform χ^2 minimization to our normalized data. In generating the Starburst99 spectra, we assumed both continuous and instantaneous star formation scenarios. We adopt a Salpeter slope for the IMF between 1 and 100 $M_{\odot}$, and ages ranging from 1 to 100 Myr. Starburst99 models were generated using libraries of empirical UV spectra from Large and Small Magallenic Cloud stars (LMC/SMC, which correspond to a metallicity $Z_{MC} \simeq 0.4\ Z_{\odot}$) and Galactic stars ($\simeq 1\ Z_{\odot}$).

Figure 5 shows two high-ionization lines associated with stellar winds used in this fit: N V λλ1238,1242 (left panels) and C IV λλ1548,1550 (middle panels). Starburst99 models are plotted for continuous (upper panels) and instantaneous (lower panels) star formation scenarios. We excluded in the fit the region encompassing the interstellar absorption in C IV, between 1543 and 1553 Å, which is not associated with the stellar P-Cygni profile.

The χ^2 ($N_{dof} = 38$) as a function of the age of the stellar population for all models is shown in the right panel of Figure 5. The model using LMC/SMG stars ($0.4\ Z_{\odot}$) with a $\sim$6 Myr old burst matches the data better ($\chi^2/N_{dof} = 39/38$), reproducing quite well both the line profiles of N V and C IV,

Table 3
Strong Interstellar Absorption Features in the Spectrum of HLock01-B

Ion	λ_{lab}	Δv	EW_0^{total}	Blue (Outflowing)			Red (Inflowing)		
				z_b	EW_0	FWHM	z_r	EW_0	FWHM
	(Å)	(km s^{-1})	(Å)		(Å)	(km s^{-1})		(Å)	(km s^{-1})
(1)	(2)	(3)	(4)	(5)	(6)	(7)	(8)	(9)	(10)
Si II	1260.42	−950 ± 750	1.94 ± 0.23	2.9503	0.69 ± 0.20	900	2.9596	1.32 ± 0.26	309
O I	1302.17	−950 ± 750	2.52 ± 0.21	⋯	⋯	⋯	2.9598	1.61 ± 0.24	373
Si II	1304.37	−950 ± 750	2.52 ± 0.21	⋯	⋯	⋯	2.9597	0.76 ± 0.12	244
C II	1334.53	−1000 ± 900	2.59 ± 0.26	2.9520	1.40 ± 0.20	898	2.9599	1.26 ± 0.12	310
Si II	1526.71	−900 ± 700	1.82 ± 0.27	2.9531	0.76 ± 0.15	740	2.9596	1.09 ± 0.16	230
Fe II	1608.45	−800 ± 950	1.27 ± 0.36[a]	⋯	⋯	⋯	2.9607[a]	1.07 ± 0.21[a]	468[a]
Al II	1670.79	−800 ± 750	1.58 ± 0.44	2.9510	0.43 ± 0.20	554	2.9599	1.16 ± 0.13	198
Si IV	1393.76	−1000 ± 650	2.25 ± 0.25	2.9520	1.71 ± 0.19	798	2.9592	0.50 ± 0.10	104
Si IV	1402.77	−1000 ± 650	1.64 ± 0.27	2.9514	1.45 ± 0.15	859	2.9599	0.29 ± 0.08	<180
C IV	1548.20	−2600 ± 1000	5.76 ± 0.40	⋯	⋯	⋯	2.9593	1.07 ± 0.40	<180
C IV	1550.78	−2600 ± 1000	5.76 ± 0.40	⋯	⋯	⋯	2.9596	0.54 ± 0.20	<180

Note. Columns are as follows: (1) and (2) ion and the corresponding vacuum wavelength; (3) velocity range for the measurements of the total rest-frame equivalent width (blueshifted and redshifted components); (4) total rest-frame equivalent width and 1σ error; (5)–(7) redshift, rest-frame equivalent width, and full width half maximum (FWHM $= 2\sqrt{2\ln 2}\,\sigma$) of the blueshifted absorption component from the Gaussian fit; (8)–(10) are the same as (5)–(7), but in this case applied to the redshifted absorption component from the Gaussian fit.
[a] The profile of Fe II $\lambda\lambda$1608 is affected by other absorption lines from an intervening system at $z = 1.4583 \pm 0.0005$.

Table 4
Metallicity Estimates Following Sommariva et al. (2012)

Index	Range (Å)	EW (Å)	$Z/Z_\odot$
F1370	1360–1380	1.4 ± 0.2	0.35
F1425	1415–1435	0.9 ± 0.1	0.28
F1460	1450–1470	1.0 ± 0.1	0.39
F1501	1496–1506	0.6 ± 0.1	0.59

Table 5
De-magnified Physical Properties of HLock01

Quantity	HLock01-B	HLock01-R	Unit
z	2.9546 ± 0.0004	2.9574 ± 0.0001	⋯
M_*	$10.1^{+0.3}_{-0.1}$	$11.7^{+0.2}_{-0.1}$	log($M_\odot$)
Age	$7.3^{+0.6}_{-0.0}$	8.6 ± 0.1	log(yr)
A_V	$0.8^{+0.1}_{-0.3}$	$4.3^{+0.4}_{-0.1}$	mag
SFR	710^{+180}_{-420}	1500 ± 200	$M_\odot$ yr^{-1}
sSFR	55^{+14}_{-27}	$2.76^{+1.22}_{-0.85}$	Gyr^{-1}
Z	0.4 ± 0.1	0.8 ± 0.2	$Z_\odot$

in particular the regions of the blueshifted absorption wind component of the C IV P-Cygni profile and its red-emission wing (regions of 1536 to 1542 and 1554 to 1563 Å, respectively). Bursts over slightly longer periods ($\lesssim$25 Myr) can also recover the stellar blueshifted absorption of C IV, but fail to reproduce the red-emission wing of HLock01-B (see the lower panels of Figure 5 for an example of a 15-Myr-old burst). However, our results should be treated with care, given the assumptions made on the slope and upper end cut-off of the IMF. Moreover, the P-Cygni profile of N V $\lambda\lambda$1238,1242 could also be affected by the red wing of the damped Lyα absorption line (see Section 3.4).

All methods used in this work to derive the metallicity of the young stars in HLock01-B point to a $Z_{stars} \simeq 0.4Z_\odot$ value. Our metallicity measurements are slightly different from the measurement of gas metallicity in HLock01-R ($0.6 < Z_{gas}/Z_\odot < 1.0$) by Rigopoulou et al. (2018), using the [O III]88/[N II]122 line ratio as a metallicity indicator. This provides additional evidence that the bright *Herschel* SMG (HLock01-R) and the bright LBG-like galaxy (HLock01-B) are likely different galaxies with distinct enrichment histories.

3.4. The Damped Lyα Profile

The Lyα line in the spectrum of HLock01-B shows a strong damped Lyα profile, with the minimum lying in the range from $\simeq$4809 to 4815 Å (or $v \simeq +100$ to $+500$ km s^{-1} relative to z_{sys}; see Figure 6). We used the software PyAstronomy[23] to generate theoretical Voigt profiles and perform χ^2 minimization to the Lyα profile. However, we noted differences in the absorption profile in the blue and red damping wings, with the absorption being more pronounced in the latter. The blue wing is more noisy and less constrained than the red one, likely due to additional absorption from the intergalactic medium in the line of sight toward HLock01-B. The red wing is well fitted with a neutral hydrogen column density $N(\mathrm{H\ I}) = (5.83 \pm 1.24) \times 10^{20}$ cm^{-2} centered at $\simeq$4813 Å or $v \simeq +370$ km s^{-1} with respect to z_{sys}. Therefore we interpret that most of the damped absorption is due to the redshifted component of the ISM seen in the spectrum of HLock01-B, which consists primarily of neutral gas and presents a large optical depth. Our derived column density of H I is in the range of typical values measured in other lensed galaxies (e.g., Pettini et al. 2000; Cabanac et al. 2008; Dessauges-Zavadsky et al. 2010).

3.5. Weak Emission Lines

As discussed in Section 3.1, the nebular C III] $\lambda\lambda$1906,1908 emission is barely detected in our OSIRIS spectrum, and the doublet is not resolved. Despite the low significance of the detection (3σ), we fit a Gaussian to the unresolved C III] doublet. We derive $z_{\mathrm{C\ III]}} = 2.954 \pm 0.002$ and $EW_0^{\mathrm{C\ III]}} = (1.0 \pm 0.3)$ Å. Other semiforbidden transitions often detected in the spectra of star-forming galaxies are the O III] $\lambda\lambda$1661,1666 lines, but these

[23] https://github.com/sczesla/PyAstronomy

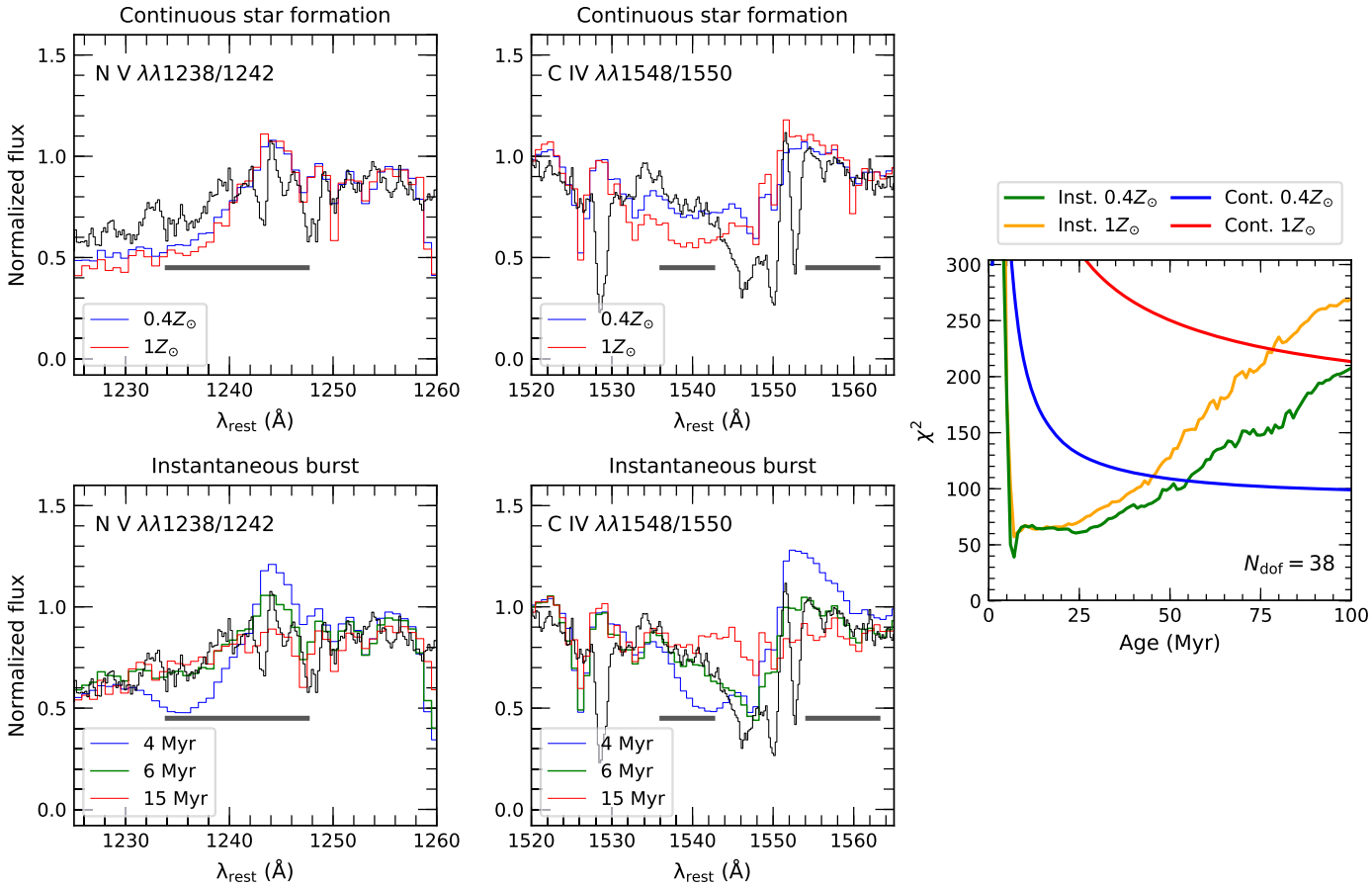

Figure 5. Comparison of the normalized spectrum of HLock01-B (black solid lines) with empirical models from STARBURST99 for high-ionization lines associated with stellar winds: N V λλ1238,1242 (left panels) and C IV λλ1548,1550 (middle panels). Upper panels show models for continuous star formation with a stellar population age $t = 100$ Myr, and for metallicities of 0.4 $Z_\odot$ (LMC/SMG stars, blue solid lines) and 1 $Z_\odot$ (Galactic stars, red solid lines). Lower panels show the comparison of the spectrum of HLock01-B with models for an instantaneous burst with $Z = 0.4$ $Z_\odot$ and ages of 4 (blue), 6 (green), and 15 (red) Myr. The wavelength windows used to perform the χ^2 minimization are marked in gray. Note that we exclude in this fit the region of strong interstellar absorption in C IV (between 1543 and 1553). The right panel shows the χ^2 ($N_{\rm dof} = 38$) as a function of the age of the stellar population for continuous and instantaneous star formation models, and metallicities of 0.4 $Z_\odot$ and 1 $Z_\odot$, as indicated. A good fit is seen for models using LMC/SMG stars (0.4 $Z_\odot$) with around 6 Myr old burst.

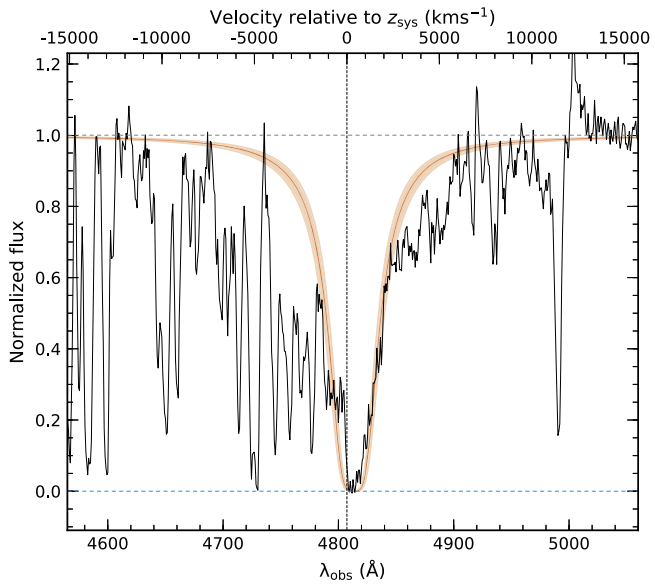

Figure 6. Portion of the spectrum of HLock01-B encompassing the region of the Lyα absorption line. The x axis is the observed wavelength (in Å) and the y axis is the normalized intensity. Overlaid is the best Voigt profile fit (red solid line) for N(H I) = (5.83 ± 1.24) × 10^{20} cm^{-2} centered at $z_{\rm Ly\alpha} = 2.9594$, as well as the 1$\sigma$ error (red filled area).

are not detected in our spectrum, despite the high continuum S/N in this spectral region (around 25). The absence of these nebular lines in HLock01-B may be due to their faintness or to contamination with the overlapping blueshifted component of the Al II λλ1670 interstellar line. In addition to C III], we also detect emission features from the excited fine-structure transitions Si II* λλ1264, 1309, and 1533. Their profiles appear slightly asymmetric (see Figure 2), with the centroids redshifted with respect to $z_{\rm sys}$ by a mean of $\simeq$+120 ± 50 km s^{-1}. This velocity offset may be due to the neighboring red component of resonance absorption features (Si II λλ1260, O I + Si II λλ1303, and Si II λλ1526), which attenuate the blue edges of the fine-structure emission profiles. We measure rest-frame equivalent widths of 0.32 ± 0.06, 0.22 ± 0.09, and 0.26 ± 0.14 Å for Si II* λλ1264,1309, and 1533, respectively.

4. Physical Properties from the Spectral Energy Distribution

Conley et al. (2011) analyzed the SED of HLock01, considering only a single lensed background source. They simultaneously fitted the emission in the optical/near-IR with longer wavelength data (far-IR and submm), but the fit did not explain the IRAC fluxes and overestimated the $K_{\rm p}$ and MIPS 70 μm flux densities by a factor of 2 or more. We now know

that HLock01 is composed of two different, spatially and spectrally offset sources, and thus the energy balance method (between dust-absorbed stellar continuum and the reprocessed dust emission in the far-IR), which was previously invoked, cannot be applied to the integrated photometry by considering a single source.

From a revised photometric analysis of both background sources, presented in Appendix B, we show that their SEDs are well defined at short (HLock01-B) and long wavelengths (HLock01-R), where these two components dominate, respectively. HLock01-B is very bright in the rest-frame UV and optical, but faint (or undetected) in the current VLA and SMA data. On the other hand, HLock01-R shows a very red and obscured counterpart in the rest-frame UV and optical, but it is very bright in the submm. However, to deblend the emission from the two components in the IRAC bands is challenging, given the limitation of the low spatial resolution. The centroids of the bright lensed images A and C seen in the IRAC 3.6 and 4.5 μm bands are slightly offset ($\simeq$0.″7) with respect to the bright counterparts in the optical and submm, suggesting a contribution of both to the total flux density in IRAC bands. However, the small rest-frame UV spectral slope of HLock01-B, $\beta = -1.9 \pm 0.1$ (measured from the observed R and I bands, and assuming a simple power law $F_\lambda = \lambda^\beta$), and the low Balmer/4000 Å break color (F110W–$K_s = 0.15$ mag), suggest that the contribution of the LBG in the mid-IR is modest compared with the emission from the SMG. Also, typical LBGs are faint in the mid-IR ($S_{24\,\mu m} \simeq 20$–$30\,\mu$Jy; Magdis et al. 2010a; Reddy et al. 2012), even those showing a redder UV β slope (Reddy et al. 2006, 2010; Coppin et al. 2007; Siana et al. 2008, 2009; Magdis et al. 2017), which are on average more massive and show larger infrared luminosities.

Additionally, in strong gravitational lensing, the finite extend of one or multiple background sources can lead to significant differential magnification, and their intrinsic properties, derived from photometric or spectroscopic diagnostics, can be incorrect if this effect is not taken into account (e.g., Hezaveh et al. 2012; Serjeant 2012). Of particular importance in treating differential magnification are the cases with multiple background sources with significantly different SEDs and positions in the source plane (e.g., the $z \sim 2.9$ gravitational lensed system analyzed in MacKenzie et al. 2014). To check this effect in HLock01, we use the high S/N and high spatial resolution *HST*/F110W imaging data to update the lens model already described in Gavazzi et al. (2011). The procedure is detailed in Appendix C. Figure 7 shows the mean positions and ellipses characterizing the galaxy shapes in the source plane for all wavebands. Stellar emission in the optical/near-IR (LBG) is coincident and slightly offset by 0.″42 ± 0.″07 in the source plane from the mutually coincident VLA, CO, and dust emission (SMG). We find magnification factors of $\mu = 8.5 \pm 0.5$ for *HST* F110W, $\mu = 8.3 \pm 0.3$ for GTC g band, $\mu = 8.2^{+0.6}_{-0.8}$ for VLA, $\mu = 9.2 \pm 0.8$ for PdBI CO ($J = 5 \rightarrow 4$), and $\mu = 9.2 \pm 0.5$ for the SMA dust continuum. The differential magnification appears to be small, since the bulk of the source emission of the LBG and SMG stands relatively far from the caustics without crossing them (see Figure 7), and thus changes of magnification as a function of source plane position vary very little. We thus assume, for simplicity, lensing magnifications of $\mu_{HST} = 8.5 \pm 0.5$ and $\mu_{SMA} = 9.2 \pm 0.5$ to be the same in the spectral range in which the LBG and the SMG are well detected, respectively.

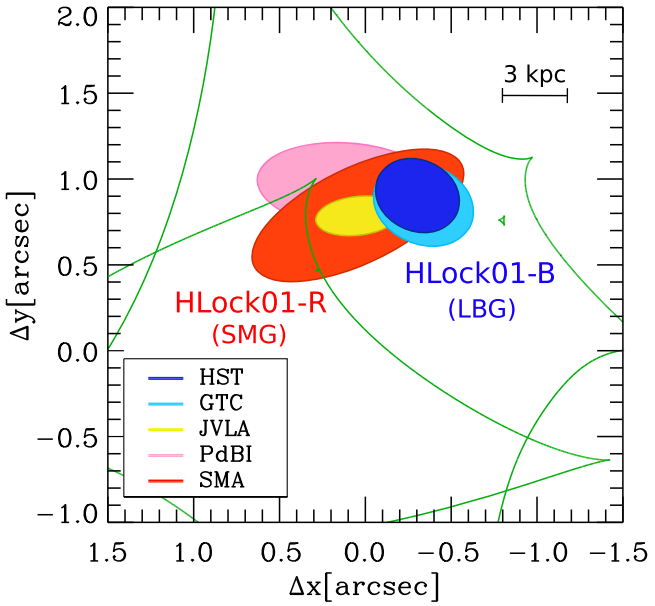

Figure 7. Source plane reconstruction of HLock01. The posterior mean effective ellipses of the reconstructed components of HLock01-B (LBG) from *HST* F110W and GTC g band are represented by blue colored ellipses. Pink, yellow, and red colored ellipses represent the effective radius of the reconstructed components of CO, VLA, and dust emission associated with HLock01-R (SMG), respectively. A relative offset of 0.″42 ± 0.″07 is seen between *HST* F110W and VLA, which corresponds to 3.3 ± 0.6 kpc.

We first used the SED-fitting code FAST (Fitting and Assessment of Synthetic Templates; Kriek et al. 2009) to derive the stellar population properties of HLock01-B. Optical U, g, R, and I, and near-IR F110W and K_s flux measurements were used in this fit (see Appendix B). We excluded fluxes from IRAC from this fit, given the uncertainties of the contribution of HLock01-B in these bands. However, the 2.2 μm K_s band corresponds to rest-frame emission at 5600 Å, above the Balmer/4000 Å break, which is sensitive to the age of the stellar population. We assume stellar population synthesis models of Bruzual & Charlot (2003), the Chabrier (2003) IMF, and an exponentially declining star formation history ($\propto e^{-t/\tau}$). We adopt a grid for the age of the stellar population, ranging from 20 Myr to the maximum age of the universe at $z \simeq 2.95$, and star formation histories with τ between 0.3 and 10 Gyr, both in steps of 0.1 dex. The attenuation curve of Calzetti et al. (2000) was adopted, and the allowed A_V range was 0–3 mag in steps of 0.05 mag. We also fixed the metallicity to $Z/Z_\odot = 0.4$, the value measured in Section 3.3 for the young O and B stars. The best-fit model ($\chi^2/N_{dof} = 1.6/3$) gives an intrinsic (i.e., corrected for the lensing magnification $\mu_{HST} = 8.5 \pm 0.5$ and assumed to be the same in the spectral range in which the LBG is well detected) stellar mass $\log(M_*/M_\odot) = 10.1^{+0.3}_{-0.1}$, and an attenuation of the stellar light of $A_V = 0.84^{+0.12}_{-0.25}$, with age $\log(\mathrm{age}_M/\mathrm{yr}^{-1}) = 7.3^{+0.6}_{-0.0}$. Errors refer to 68% confidence intervals derived using 500 Monte Carlo simulations. After correction for the lensing magnification, the star formation rate of the best-fit model is $\mathrm{SFR} = 710^{+180}_{-420}\,M_\odot\,\mathrm{yr}^{-1}$.

We further performed a multiband SED fit of HLock01-R using the high-z extension of MAGPHYS (Multi-wavelength Analysis of Galaxy Physical Properties; da Cunha et al. 2008, 2015) to explore its SFR, and stellar and dust mass (M_d). MAGPHYS uses the Bruzual & Charlot (2003) stellar populations with a Chabrier (2003) IMF and assumes the attenuation model of Charlot & Fall

Table 6
Photometry of HLock01

Telescope/Detector	λ (μm)	HLock01-B[a] (LBG)	HLock01-R[a] (SMG)	Units	References
CFHT/MEGACAM (*U*)	0.38	8.2 ± 0.6	⋯	μJy	⋯
GTC/OSIRIS (*g*)	0.48	29.7 ± 0.8	⋯	μJy	⋯
INT/WFC (*R*)	0.63	46.5 ± 0.6	⋯	μJy	Conley et al. (2011)
Subaru/SuprimeCam (*I*)	0.76	47.9 ± 0.04	⋯	μJy	Conley et al. (2011)
HST/F110W	1.16	53.5 ± 2.5	2.3 ± 0.6	μJy	
WHT/LIRIS (K_s)	2.20	60.8 ± 4.7[b]	16.3 ± 3.8[b]	μJy	⋯
Spitzer/IRAC (I1)	3.6	74 ± 9[c]	82 ± 9[d]	μJy	⋯
Spitzer/IRAC (I2)	4.5	75 ± 11[c]	113 ± 11[d]	μJy	⋯
Spitzer/IRAC (I3)	5.8	76 ± 20[c]	219 ± 20[d]	μJy	⋯
Spitzer/IRAC (I4)	8.0	63 ± 20[c]	341 ± 20[d]	μJy	⋯
Spitzer/MIPS	24	⋯	1.24 ± 0.02	mJy	Wardlow et al. (2013)
Spitzer/MIPS	72	⋯	16.1 ± 0.3	mJy	Wardlow et al. (2013)
Spitzer/MIPS	160	⋯	244.4 ± 1.4	mJy	Wardlow et al. (2013)
Herschel/SPIRE	250	⋯	403 ± 7	mJy	Wardlow et al. (2013)
Herschel/SPIRE	350	⋯	377 ± 10	mJy	Wardlow et al. (2013)
Herschel/SPIRE	510	⋯	249 ± 7	mJy	Wardlow et al. (2013)
SMA	880	⋯	52.8 ± 0.5	mJy	Conley et al. (2011)
CSO/Z-Spec	1000–1100	⋯	27.5 ± 0.6	mJy	Conley et al. (2011)
CSO/Z-Spec	1100–1200	⋯	20.4 ± 0.5	mJy	Conley et al. (2011)
CSO/Z-Spec	1200–1300	⋯	16.2 ± 0.5	mJy	Conley et al. (2011)
CSO/Z-Spec	1300–1400	⋯	12.0 ± 0.5	mJy	Conley et al. (2011)
CSO/Z-Spec	1400–1500	⋯	9.9 ± 0.6	mJy	Conley et al. (2011)
CARMA	3400	⋯	0.61 ± 0.19	mJy	Conley et al. (2011)
VLA	214000	⋯	0.97 ± 0.05	mJy	Wardlow et al. (2013)

Notes.
[a] Total flux densities of the four lensed components, uncorrected for lensing magnification.
[b] Obtained by modeling the light profiles using GALFIT.
[c] Expected *Spitzer*/IRAC fluxes of HLock01-B, extrapolated from the best-fit SED using flux measurements from 0.38 to 2.20 μm (see Section 4).
[d] Refers to the difference between the total flux densities measured in Appendix B (156, 188, 295, and 404 μJy for the *Spitzer*/IRAC bands I1, I2, I3, and I4, respectively) and the expected flux densities of HLock01-B from the best-fit SED.

(2000). We used the flux measurements from 1.1 μm to radio. In the *Spitzer*/IRAC bands, we used the difference between the total fluxes (measured in Appendix B) and the expected flux of HLock01-B from the best-fit SED, as indicated in Table 6. The best-fit model (reduced $\chi^2 = 3.1$) gives a lensing corrected ($\mu_{\rm SMA} = 9.2 \pm 0.5$) stellar mass $\log(M_*/M_\odot)=11.7^{+0.2}_{-0.1}$, a mass weighted age $\log({\rm age}_M/{\rm yr}) = 8.6 \pm 0.1$, and a large attenuation $A_V = 4.26^{+0.35}_{-0.10}$ mag. We find a dust mass $\log(M_{\rm d}/M_\odot) = 8.8 \pm 0.1$, with a dust temperature $T_{\rm d} = (53.6 \pm 0.2)$ K. The uncertainties are derived from the 16th and 84th percentiles. The best-fit SED also yields an intrinsic total infrared luminosity $L_{\rm IR} = (1.5 \pm 0.1) \times 10^{13} L_\odot$, which is defined as the luminosity from 8 to 1000 μm in the rest frame. Using a Kennicutt relation (Kennicutt 1998) with a Chabrier IMF (Chabrier 2003), the total infrared luminosity implies a star formation rate of $\simeq 1500\, M_\odot\, {\rm yr}^{-1}$. All values were corrected for the lensing magnification derived from the SMA 880 μm data ($\mu_{\rm SMA} = 9.2 \pm 0.5$), which for simplicity, we assume to be the same from the observed near-IR to submm bands for HLock01-R.

We followed Delvecchio et al. (2017) and Miettinen et al. (2017) to look for a possible AGN contribution in HLock01-R. We use the three-component fitting code SED3FIT (Berta et al. 2013), which accounts simultaneously for stellar, dust, and AGN emission. However, the stellar and dust components of SED3FIT use the model libraries of da Cunha et al. (2008), rather than the ones used in the new high-z extension of MAGPHYS (da Cunha et al. 2015), which are expected to be better suited for high-z SMGs. We found a poor fit to our data with a $\chi^2 = 15.4$ for the best-fit model, which is much higher than the χ^2 of the standard MAGPHYS fit. Nevertheless, the mean AGN contribution to the total $L_{\rm IR}$ was found to be 1%, and less than 20% in the IRAC bands. Our analysis does not completely exclude the possibility that HLock01-R may harbor an AGN (see also Conley et al. 2011; Riechers et al. 2011; Scott et al. 2011; Magdis et al. 2014, for a discussion of the presence of an AGN in HLock01), but its contribution to the total $L_{\rm IR}$ and M_* is not substantial, as also pointed out by Rigopoulou et al. (2018).

Figure 8 shows our best-fit SED models for HLock01-B (FAST) and HLock01-R (MAGPHYS). Our results show that both galaxies are undergoing simultaneous episodes of star formation activity (unobscured, nearly dust-free in HLock01-B, and dust-enshrouded star formation in HLock01-R), but they are physically very distinct. While HLock01-R is a very massive galaxy with an evolved stellar population, HLock01-B appears to be a young, lower-mass satellite of HLock01-R.

5. Discussion

5.1. Close Merger or a Large Rotational Disk?

Our high S/N GTC/OSIRIS spectrum of the optically bright lensed images of HLock01 (HLock01-B) shows several

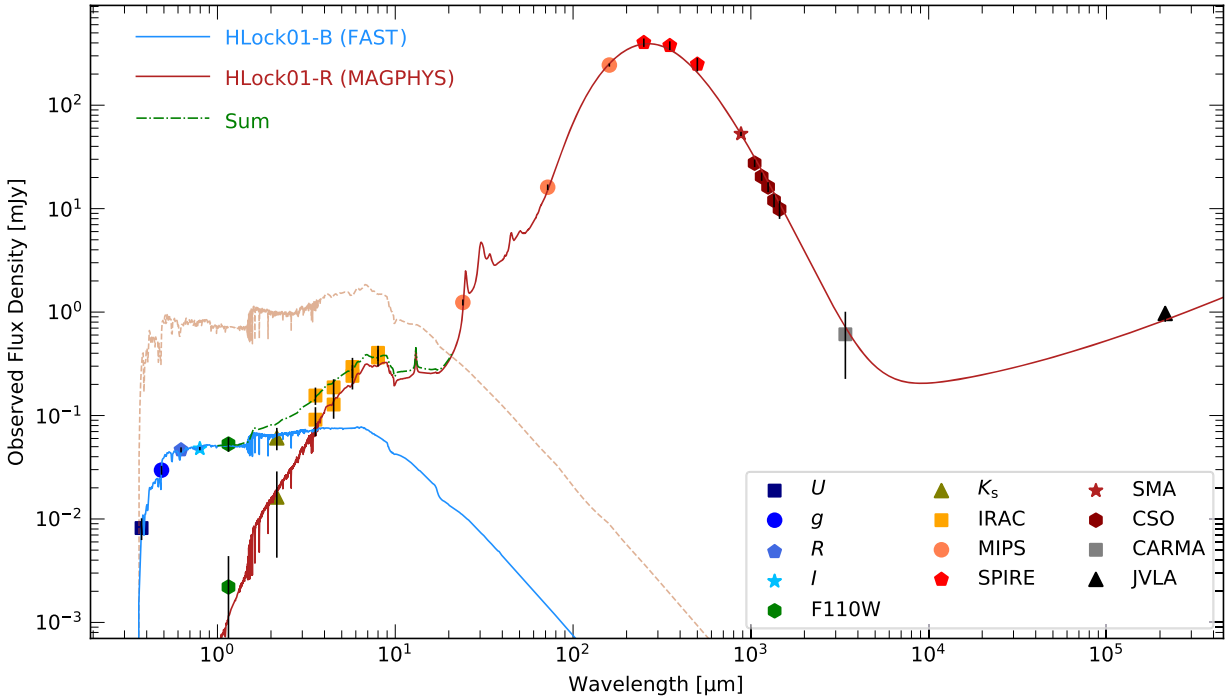

Figure 8. Best-fit model of the spectral energy distribution of HLock01-B (LBG, blue solid line) using FAST (Kriek et al. 2009), and HLock01-R (SMG, red solid line) using MAGPHYS (da Cunha et al. 2008, 2015). The LBG fit uses photometry from CFHT U to WHT K_s bands, whereas for the SMG the fit uses photometry from the rest-frame UV (*HST* WFC3 F110W) to radio. We also used the estimated fluxes in the *Spitzer* bands (3.6, 4.5, 5.8, and 8.0 μm), as explained in the text. The unattenuated SED of the SMG is plotted as a red dashed line.

well-defined UV photospheric absorption lines, for which we secured the systemic redshift $z_{\rm sys} = 2.9546 \pm 0.0004$. This value differs by $-210\,{\rm km\,s^{-1}}$ from the redshift of HLock01-R measured from the molecular gas lines $z_{\rm CO} = 2.9574 \pm 0.0001$ (Riechers et al. 2011; Scott et al. 2011). A spatial offset of 3.3 kpc (in projection) has also been found in the source plane between the bulk of the stars that emit at rest-frame UV/optical wavelengths (HLock01-B), and the molecular gas and dust distribution associated with the luminous far-IR emitting source HLock01-R.

Although similar or even larger rotational velocities have been found in massive disk SMGs at high-z (e.g., Carilli et al. 2010; Daddi et al. 2010; Jiménez-Andrade et al. 2017; Jones et al. 2017), a scenario with HLock01-B being a dust-free region, that is part of a large rotational disk of HLock01-R, is unlikely. Such asymmetry in the dust distribution, with the lack of dust attenuation in HLock01-B, would be difficult to explain. Additionally, despite the large errors, the differences in the metallicity measured in the stars of HLock01-B and in the gas of the *Herschel* SMG HLock01-R (Rigopoulou et al. 2018) suggest they are different galaxies with different enrichment histories.

Therefore, bringing together our GTC spectroscopic results and the complex velocity structure seen in the molecular gas reservoir in HLock01-R (Riechers et al. 2011), we argue that HLock01 comprises two close but different sources, forming a pair of merging galaxies (HLock01-B and HLock01-R) separated by 3.3 kpc in projection. The merger scenario is also sustained by the broadness of the blueshifted ISM absorption lines seen in the spectrum of HLock01-B, suggesting highly turbulent gas likely produced by the close merger. While HLock01-R appears to be an evolved massive galaxy with a very large obscured star formation rate, HLock01-B is a young lower-mass satellite galaxy with photometric properties similar to those of LBGs, yet undergoing a young burst ($\gtrsim$6 Myr) of star formation, likely triggered by the gravitational interaction with the nearby massive SMG.

It is worth mentioning that without the gravitational lensing effect, our results could easily be mistaken. First, without the magnification in the apparent flux of HLock01-B, the systemic redshift, measured from faint stellar photospheric lines, would be difficult to obtain. In the absence of strong UV nebular emission lines, as is the case of HLock01-B, a significant continuum S/N is required to detect faint photospheric absorption lines. second, the projected 3.3 kpc spatial offset seen between the two different objects in the source plane would correspond to only $0\farcs4$ without the lensing distortion, which is challenging to observe due to the limitation on the spatial resolution and sensitivity of current instruments.

It is thus no surprise that most high-z close mergers ($\lesssim$10 kpc projected separation) have been discovered through the gravitational lensing effect (e.g., Ivison et al. 2010b; MacKenzie et al. 2014; Messias et al. 2014; Rawle et al. 2014; Wuyts et al. 2014; Spilker et al. 2015; Marrone et al. 2018), with a few exceptions of unlensed, well separated, SMG–SMG, SMG-QSO or SMG-LBG bright interacting pairs resolved with interferometric observations (e.g., Ivison et al. 2002, 2008; Smail et al. 2003; Salomé et al. 2012; Oteo et al. 2016; Lu et al. 2017; Riechers et al. 2017).

5.2. Outflow/Inflowing Gas

Turning to the rest-frame UV spectral features, the internal kinematics of HLock01-B are very complex and different from what is observed in typical LBGs, showing two distinct components of the ISM. The blueshifted component of the ISM

is centered at $v_{\rm ISM} \simeq -220\,{\rm km\,s^{-1}}$ relative to the stars, which we associate with galaxy-scale outflows of material via stellar and supernova-driven winds, as seen in many other high-z star-forming galaxies (e.g., Shapley et al. 2003; Steidel et al. 2010). This component is stronger (i.e., larger equivalent widths) in high-ionization lines, like Si IV and C IV, similar to what is found in other young, low-metallicity galaxies (e.g., Erb et al. 2010; James et al. 2014). It is also detected in some low-ionization lines, but with a much broader profile (FWHM $\simeq 900\,{\rm km\,s^{-1}}$) than in typical LBGs ($\simeq$560 $\rm km\,s^{-1}$; Shapley et al. 2003; Steidel et al. 2010), extending over a large velocity range from approximately -1000 to $+600\,{\rm km\,s^{-1}}$. We interpret that the broadness of the blueshifted absorption lines in HLock01-B is the result of a combination of strong winds of massive stars in the LBG and a complex velocity structure due to the close gravitational interaction with the massive SMG.

On the other hand, the redshifted component seen in all strong absorption lines (see Figures 3 and 4) is highly unusual and not seen in the many high-z galaxies studied (e.g., Shapley et al. 2003; Steidel et al. 2010). This component can be understood as gas apparently moving toward the young stars of HLock01-B, because the absorbing gas must lie in front of the LBG. We relate this component with the large column density of foreground neutral gas (N(H I) $= (5.83 \pm 1.24) \times 10^{20}\,{\rm cm^{-2}}$), giving rise to the damped Lyα absorption seen in the spectrum of HLock01-B (see Section 3.4). The detection of this absorption in both low- and high-ionization ISM lines also suggests that the gas has a broad range of temperatures, from cold, mostly neutral (e.g., O I), to warmer and ionized gas (e.g., Si IV, and C IV).

The origin and nature of the redshifted component seen in all strong absorption lines in the spectrum of HLock01-B is unclear, and with the available data we cannot arrive at a definite conclusion. Interpreting the redshifted component also depends strongly on the spatial location of the SMG and LBG along our line of sight. The relatively low dust attenuation in HLock01-B ($A_{\rm V} = 0.8^{+0.1}_{-0.3}$) may suggest that the SMG is located in the background; otherwise the stellar continuum of the LBG would be highly attenuated by the foreground dust content of HLock01-R (see Figure 7). Therefore it is unlikely that the redshifted component is associated with outflows from HLock01-R or rotating gas in its disk seen from the background HLock01-B.

In this sense, the redshifted component could be associated with a dwarf galaxy or a damped Lyα system falling toward HLock01. Gas ejected by a previous episode of star formation or AGN activity in HLock01 would not easily escape its intense gravitational pull. If cooled enough, these reservoirs of gas would provide additional fuel to prolong the star formation activity (e.g., Davé et al. 2011; Hopkins et al. 2014; Narayanan et al. 2015; Wang et al. 2015; Emonts et al. 2016). Assuming that the gas is dynamically linked and collapsing toward HLock01, it is more likely that the gas is falling into the massive SMG with $v \simeq +170\,{\rm km\,s^{-1}}$, instead of falling to HLock01-B with $v \simeq +370\,{\rm km\,s^{-1}}$, which seems too high for a $10^{10}\,M_{\odot}$ galaxy.

Evidence of accretion of cool, metal-enriched gas has been found in only a few spectra of star-forming galaxies at moderately low-z (e.g., Sato et al. 2009; Coil et al. 2011; Martin et al. 2012; Rubin et al. 2012), and is more elusive at high-z (e.g., Bouché et al. 2013; Wiseman et al. 2017) due to the faintness of individual high-z galaxies. Some authors suggest that the low detection rate of infalling gas is due to the geometry and alignment of the streams, which can only be detected in absorption if favorably aligned with our line of sight (Kimm et al. 2011; Martin et al. 2012). Nevertheless, accretion of cold gas, either in the form of cold flows, mergers, or recycled gas from stellar feedback, plays an important role in star formation histories and galaxy growth.

5.3. Extended Gas Reservoir?

We reported an unusual absorption line at $\simeq$5281 Å in the red wing of a bright Lyα emission at $z \simeq 3.327$, associated with an object 14″ SW of HLock01 (see Appendix A). This absorption is consistent with C II $\lambda\lambda$1334 at $z = 2.9574 \pm 0.0008$, very close by $\Delta v = (-8 \pm 76)\,{\rm km\,s^{-1}}$ to the redshift of HLock01-R measured from the molecular gas ($z_{\rm CO} = 2.9574 \pm 0.0001$). The limited spectral coverage of the Lyα emission line and the faintness of the continuum associated with the $z \simeq 3.327$ galaxy does not let us unambiguously confirm if the absorption line is C II at the redshift of HLock01-R, or a different absorption line system at a lower redshift. If related with HLock01-R, it may suggest a substantial gas reservoir in the halo at an impact parameter of 110 kpc. It is worth noting that Fu et al. (2016) used QSO absorption line spectroscopy in three high-z SMG-QSO close pairs, with the QSO at a larger redshift than the SMG, to probe the circumgalactic medium (CGM) at similar impact parameters. However, they did not find evidence of optically thick H I gas or strong neutral absorbers in the CGM. Our results suggest that at least massive SMGs, such as HLock01-R, may have prominent cool gas reservoirs in their halos that could fuel a prolonged star formation phase.

5.4. Physical Properties

The intrinsic physical properties (corrected for lensing magnification) derived from multiband SED fitting reveal that HLock01-R is a far-IR luminous SMG (as already discussed in earlier papers; e.g., Conley et al. 2011; Wardlow et al. 2013), with an ongoing SFR $\simeq 1500\,M_{\odot}\,{\rm yr^{-1}}$, but yet heavily obscured at short wavelengths. Our new analysis reveals a large, highly obscured stellar mass, similar to the most massive and extreme SMGs during the peak of star formation (e.g., Hainline et al. 2011; Ma et al. 2015; Schinnerer et al. 2016; Miettinen et al. 2017; Nayyeri et al. 2017). However, as already discussed in Conley et al. (2011) and Wardlow et al. (2013), HLock01-R has a moderately low $q_{\rm IR} = 1.8 \pm 0.4$ (which is the logarithmic ratio of $L_{\rm IR}$ and the rest-frame 1.4 GHz flux density), compared with the mean value for HerMES sources ($q_{\rm IR} = 2.40 \pm 0.12$; Ivison et al. 2010a). This may indicate a hidden, radio emitting AGN, but from our SED analysis in Section 4, we have shown that if HLock01-R harbors an AGN, its contribution to the total $L_{\rm IR}$ and SFR is modest ($\simeq$1%), as also noted by Rigopoulou et al. (2018), and even assuming a maximum of 20% of an AGN contribution to the IRAC fluxes, the stellar mass of HLock01-R will be lower only by 0.1 dex, which is within our measurement errors. Moreover, Hayward & Smith (2015) have also shown that the physical properties derived using MAGPHYS are robust even when the AGN contributes 25% of the total UV to IR luminosity. Our deep GTC/OSIRIS rest-frame UV spectroscopy does not show any line or continuum emission at the positions of the lensed

images of HLock01-R, as some of them are included in the regions covered by our long-slit spectra (see Figure 1, left panel). However, follow-up observations are required to constrain the presence of an AGN in HLock01-R. Nevertheless, even assuming a small AGN contribution, our results show that HLock01-R has already formed the majority of its stellar content, with a gas mass fraction of $f_{\rm gas} \equiv M_{\rm gas}/M_* = 0.07 \pm 0.02$ (for $M_{\rm gas} = 3.3 \times 10^{10}\,M_\odot$, as measured in Riechers et al. 2011), a specific star formation rate sSFR $\equiv$ SFR$/M_* = 2.76^{1.22}_{-0.85}$ Gyr^{-1}, and a depletion timescale ($\tau_{\rm d} \equiv M_{\rm gas}/{\rm SFR}$) of only 22 Myr (assuming no gas input). Moreover, it is plausible that additional gas input from the ongoing merger and inflows of material from a substantial gas reservoir in the halo will extend the starburst phase of HLock01 for a prolonged time, becoming an even more massive elliptical galaxy in the local universe.

On the other hand, HLock01-B appears to be a young, lower-stellar mass galaxy with very different properties than HLock01-R. In the optical, it is one of the brightest gravitationally lensed high-z star-forming galaxies known so far (e.g., Yee et al. 1996; Allam et al. 2007; Belokurov et al. 2007; Smail et al. 2007; Lin et al. 2009; Wuyts et al. 2010; Bayliss et al. 2011; Dahle et al. 2016; Marques-Chaves et al. 2017), with an apparent total magnitude of $R = 19.73 \pm 0.01$. Even after accounting for the magnification produced by the lensing group of galaxies ($\mu_{HST} = 8.5 \pm 0.5$), it is still very luminous in the rest-frame UV with an absolute magnitude $M_{\rm UV} = -23.4$, two-and-a-half magnitudes more luminous than typical LBGs ($L^*_{\rm UV}$) at a similar redshift (Reddy & Steidel 2009). The stellar mass and SFR derived in Section 4 yield a specific star formation rate of 55 Gyr^{-1} well above the main sequence at that redshift (e.g., Mannucci et al. 2009; Magdis et al. 2010b; Álvarez-Márquez et al. 2016). The nature and properties of this kind of UV ultraluminous galaxies (i.e., $M_{\rm UV} \lesssim -23$) are still poorly understood, given the lack of examples reported in the literature (e.g., Allam et al. 2007; Bian et al. 2012; Le Fèvre et al. 2013; Marques-Chaves et al. 2017; Ono et al. 2017). This is due in part to the fact that this kind of galaxy is extremely rare, and finding them requires wider-field surveys with deep, multiband observations. The high UV luminosities also place these sources in the transition between luminous galaxies and faint AGNs, needing either extensive multi-wavelength imaging (e.g., X-ray, mid-IR, and radio) or spectroscopic follow-up. However, we stress that the unusual kinematics of the ISM and its high UV luminosity and SFR are not representative of the $z \sim 3$ LBG population. Our results suggest that the gravitational interaction with the massive SMG may have triggered the larger UV luminosity and SFR. The interaction may also be the origin of the large obscured SFR and far-IR luminosity in the SMG. Despite this, HLock01-B shares many of its properties with the population of $z \sim 3$ LBGs. Its UV colors, $(G - R) \simeq 0.5$ and $(U - G) \simeq 1.4$, are consistent with the standard color selection criteria of $z \sim 3$ LBGs (Steidel et al. 1996, 2003). However, HLock01-B presents $(R - K) = 0.29 \pm 0.07$, bluer than typical $z \sim 3$ LBGs ($(R - K) \simeq 1.0$; Shapley et al. 2001), and Lyα emitting galaxies ($(R - K) \simeq 0.4$; Ono et al. 2010).

Table 5 summarizes the main physical properties of both components of HLock01.

6. Summary and Conclusions

We have presented a detailed study of HLock01, one of the first gravitational lensed sources discovered in the HerMES survey. Unlike other SMGs, HLock01 is apparently very bright in all observed spectral bands, even in the optical. It is magnified by a factor of around 9 by a galaxy group-scale dark matter halo at $z = 0.645$ and comprises four images in the observed plane. We have used OSIRIS on the GTC to secure a high S/N ($\simeq$30) rest-frame UV spectrum of the optically bright lensed images of HLock01, with an intermediate resolution ($\simeq$180 km s^{-1}), covering the wavelength interval 1150–1950 Å in the rest-frame. From the analysis of these data together with other existing observations of HLock01, we arrive at the following main results.

1. We measured the systemic redshift of the optically bright lensed images of HLock01 (HLock01-B) $z_{\rm sys} = 2.9546 \pm 0.0004$ using weak stellar photospheric lines. This value is offset by -210 km s^{-1} from the redshift measured previously from the molecular gas lines $z_{\rm CO} = 2.9574 \pm 0.0001$ associated with the luminous far-IR source of HLock01 (HLock01-R). Our results show that the dust-obscured, far-IR emitting source HLock01-R, and the optically bright source HLock01-B, are most likely different galaxies undergoing a close merger or an interacting pair separated by only 3.3 kpc in projection.
2. We find a stellar metallicity for the stars in HLock01-B $Z_{\rm stars} \simeq 0.4\,Z_\odot$ based on two independent methods: blends of stellar photospheric lines and P-Cygni profiles from the most luminous O and B stars. This value differs slightly from that measured for the gas in HLock01-R ($0.6 < Z_{\rm gas}/Z_\odot < 1.0$), based on far-IR fine-structure line ratios. A young ($\gtrsim$6 Myr) starburst model with a Salpeter IMF, stellar masses from 1 to 100 $M_\odot$, and an LMC/SMC metallicity explains well the properties of the high-ionization lines in HLock01-B.
3. The interstellar absorption lines in the spectrum of HLock01-B exhibit two distinct components. One is blueshifted by -220 km s^{-1} relative to the stars of HLock01-B, which we associate with galaxy-scale outflows via stellar and supernovae driven winds. However, it also shows a broader profile (FWHM $\simeq$ 900 km s^{-1}) than in most star-forming galaxies at $z = 2$–3, indicating highly turbulent kinematics of the outflowing gas likely due to the close merger. This component is stronger in high-ionization lines, suggesting that the gas is mostly ionized or the neutral gas has a lower covering factor than the ionized gas.

   Another absorption component is seen in the spectrum of HLock01-B, but is redshifted relative to either HLock01-B and HLock01-R by +370 and +170 km s^{-1}, respectively, which can be understood as gas moving toward both galaxies. We relate this component with the strong damped Lyα line seen in HLock01-B, with a column density of $N({\rm H\,I}) = (5.83 \pm 1.24) \times 10^{20}$ cm^{-2}. Although with the available data we cannot arrive at a definitive conclusion on its nature and origin, we interpret this absorption feature as gas falling toward HLock01-R, which is more massive, with $v \simeq 170$ km s^{-1}, but viewed in absorption along a favorable line of sight toward HLock01-B. This component is detected in both low- and

high-ionization interstellar lines, but with slightly different absorption line profiles, suggesting that the gas has a broad range of temperatures, and possibly different origin.

4. We detected an unusual absorption line in the red wing of the bright Lyα emission at $z \simeq 3.327$ at 14″ SW from the lensing galaxy G1, which we tentatively associate with C II $\lambda\lambda$1334 at the redshift of HLock01-R. If this absorption is related with HLock01-R and not with an absorbing system at a different redshift, it indicates a substantial gas reservoir in the halo of HLock01 at a projected distance of 110 kpc. Additionally, we report a broad absorption line QSO at a projected distance of 2.5 Mpc from HLock01, with a redshift very close to HLock01-R ($\Delta v \simeq 300\,\mathrm{km\,s^{-1}}$).
5. Our revised SED fitting with two different galaxies, one very bright in the optical and the other in the far-IR, implies that both are physically very distinct. HLock01-B appears to be a young, lower-mass satellite galaxy of HLock01-R, undergoing an intense episode of star formation activity likely triggered by the interaction. HLock01-R shows an already evolved stellar population, and its high stellar mass in combination with the low gas fraction suggests that the SMG has already assembled most of its stellar mass. However, additional gas input from the satellite galaxy HLock01-B and from the reservoir of gas around HLock01-R may extend the starburst phase of the SMG, eventually forming one of the most massive galaxies in the local universe.

We would like to thank the anonymous referee for their suggestions, which significantly improved the clarity of this paper. We also thank Alice Shapley for allowing us to use their rest-frame UV composite spectrum of LBGs and Helmut Dannerbauer for useful discussions. Based on observations made with the Gran Telescopio Canarias (GTC) and with the William Herschel Telescope (WHT), both installed in the Spanish Observatorio del Roque de los Muchachos of the Instituto de Astrofísica de Canarias, on the island of La Palma. We thank the GTC and WHT staff for their help with the observations. R.M.C. acknowledges Fundación La Caixa for the financial support received in the form of a PhD contract. R.M.C., I.P.F., P.M.N., and C.J.A. acknowledge support from the Spanish Ministerio de Economia y Competitividad (MINECO) under grant number ESP2015-65597-C4-4-R. Y.S. has been partially supported by the 973 program (No. 2015CB857003) and the National Natural Science Foundation of China (NSFC) under grant numbers 11603032 and 11333008. J.L.W. gratefully acknowledges an STFC Ernest Rutherford Fellowship and additional support from STFC (ST/P000541/1).

SPIRE has been developed by a consortium of institutes led by Cardiff University (UK) and including Univ. Lethbridge (Canada); NAOC (China); CEA, LAM (France); IFSI, Univ. Padua (Italy); IAC (Spain); Stockholm Observatory (Sweden); Imperial College London, RAL, UCL-MSSL, UKATC, Univ. Sussex (UK); and Caltech, JPL, NHSC, Univ. Colorado (USA). This development has been supported by national funding agencies: CSA (Canada); NAOC (China); CEA, CNES, CNRS (France); ASI (Italy); MCINN (Spain); SNSB (Sweden); STFC, UKSA (UK); and NASA (USA).

Funding for SDSS-III has been provided by the Alfred P. Sloan Foundation, the Participating Institutions, the National Science Foundation, and the U.S. Department of Energy Office of Science. The SDSS-III website is http://www.sdss3.org/. SDSS-III is managed by the Astrophysical Research Consortium for the Participating Institutions of the SDSS-III Collaboration, including the University of Arizona, the Brazilian Participation Group, Brookhaven National Laboratory, Carnegie Mellon University, University of Florida, the French Participation Group, the German Participation Group, Harvard University, the Instituto de Astrofisica de Canarias, the Michigan State/Notre Dame/JINA Participation Group, Johns Hopkins University, Lawrence Berkeley National Laboratory, Max Planck Institute for Astrophysics, Max Planck Institute for Extraterrestrial Physics, New Mexico State University, New York University, Ohio State University, Pennsylvania State University, University of Portsmouth, Princeton University, the Spanish Participation Group, University of Tokyo, University of Utah, Vanderbilt University, University of Virginia, University of Washington, and Yale University.

Facilities: GTC (OSIRIS), *HST* (WFC3), WHT (LIRIS), *Spitzer* (IRAC), *Herschel* (SPIRE), SMA, VLA.

Appendix A
Environment of HLock01

We serendipitously detected in two of our 1.″2-wide GTC long-slit spectra (PA = −39.°5 and 44°) three strong, asymmetric lines that we interpret as Lyα emission at $z = 2.721 \pm 0.001$, $z = 3.145 \pm 0.001$, and $z = 3.327 \pm 0.001$, at 2.′37, 4.′35, and 14″ from the lensing galaxy G1, respectively. Figure 9 shows the profiles of the Lyα emission, as well as the coordinates and magnitudes of the associated objects seen in CFHT *R* band data.

In particular, the Lyα emission at $z = 3.327$ shows a broad profile (FWHM $\simeq 1000\,\mathrm{km\,s^{-1}}$, after accounting for the instrumental broadening), and has an observed flux of $F_{\mathrm{Ly}\alpha} = (1.38 \pm 0.2) \times 10^{-15}\,\mathrm{erg\,s^{-1}\,cm^{-2}}$. A more detailed analysis of this object will be presented in R. Marques-Chaves et al. (2018, in preparation), based on recent observations with GTC. We noticed that the red wing of the Lyα emission shows an unusual and unresolved (FWHM $< 180\,\mathrm{km\,s^{-1}}$) absorption line at 5281.2 ± 0.9 Å (see Figure 9, bottom right corner), which is not related to this galaxy. This could be an absorption system at any lower redshift, but surprisingly it is consistent with C II $\lambda\lambda$1334 absorption at $z = 2.9574 \pm 0.0008$, very close ($\Delta v = -8 \pm 76\,\mathrm{km\,s^{-1}}$) to the redshift of HLock01-R measured from the molecular gas ($z_{\mathrm{CO}} = 2.9574 \pm 0.0001$; Riechers et al. 2011; Scott et al. 2011). If this absorption is physically related to HLock01, it may suggest a substantial gas reservoir in its halo, at an impact parameter $b = 110$ kpc.

We also report on a $z = 2.961$ quasar, SDSS J105715.48 +573324.3, at 5.′5 NW from HLock01 (see Figure 9 at the top right corner). This object was cataloged as a broad absorption line quasar (BAL QSO) by Trump et al. (2006) from the third edition of the Sloan Digital Sky Survey (SDSS; York et al. 2000) Quasar Catalog (Schneider et al. 2005). The redshift of this BAL QSO is very close to the one of HLock01-R ($\Delta v \simeq 300\,\mathrm{km\,s^{-1}}$) and is located at a projected distance of 2.5 Mpc.

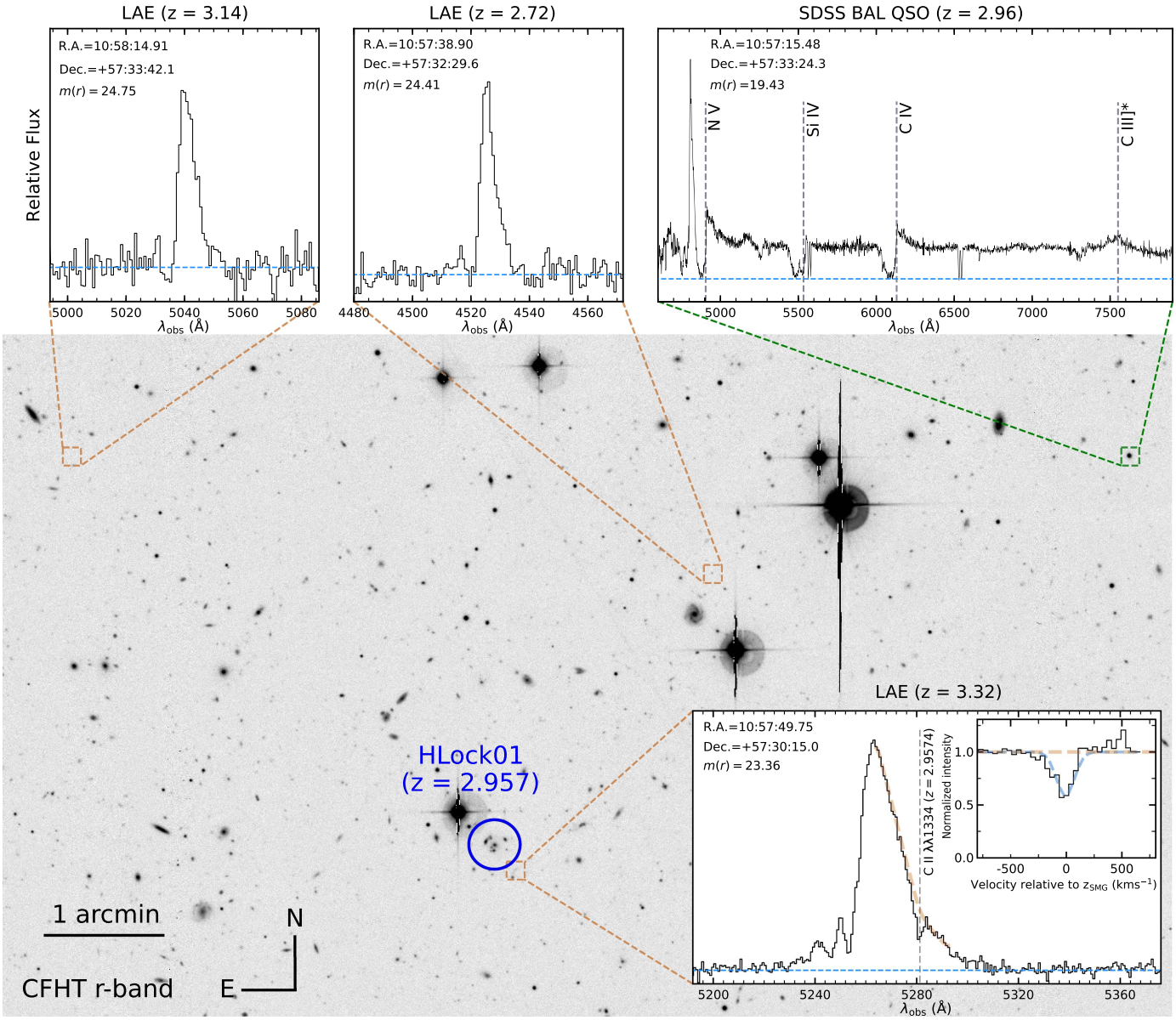

Figure 9. CFHT *R* band showing the spatial distribution of the $z \simeq 2.96$ BAL QSO SDSS J105715.48+573324.3 (top right corner, green dashed square), and three high-redshift galaxies (LAEs) serendipitously detected in two of our GTC long-slit spectra (red dashed squares). The position of HLock01 is marked in blue. The redshift of the Lyα lines, as well as the coordinates and *R* band magnitudes of the associated objects, are labeled in each panel. In particular, the $z = 3.327$ Lyα emission (bottom right corner) shows an unresolved absorption line at 5281 Å in its red wing. This absorption is consistent with the low-ionization line C II $\lambda\lambda$1334 at $z = 2.9574 \pm 0.0008$ (inset panel), very close ($\Delta v = -8 \pm 76$ km s^{-1}) to the redshift of HLock01-R measured from the molecular gas ($z_{\rm CO} = 2.9574 \pm 0.0001$; Riechers et al. 2011; Scott et al. 2011).

Appendix B
Broadband Photometry

In addition to the photometry presented in Conley et al. (2011) and Wardlow et al. (2013), we also performed photometry on the new imaging data. These measurements are summarized in Table 6.

We use aperture photometry in the *U* band from the corresponding CFHT/MEGACAM catalog, which contains detections of all four lensed images, since the light contamination from the red, lensing galaxies is negligible in *U* band. For GTC *g* band, we applied aperture photometry on the lensed images A, C, and D. We exclude photometry of the lensed image B, as it is strongly blended with the lens galaxy G4, but we use the lens model to correct for the omitted light from image B (a roughly 15% correction).

Despite the short exposure time of the *HST* F110W data, faint emission is seen close to the radio and submm lensed images A and C (see Figure 10). *K* band imaging from WHT/LIRIS and NIRC2/Keck-II (the latter discussed in Gavazzi et al. 2011; Calanog et al. 2014) also reveal faint emission at these positions. The red colors from the optical to 2.2 μm imaging seen in Figure 10 (left panel) and Table 6 suggest that this faint emission corresponds to the obscured rest-frame UV and optical light of the *Herschel* SMG. Associating this faint emission to HLock01-R, we measure the flux in a small aperture (0.″77 diameter) at the position of the faint near-IR source detected close to the radio and submm lensed image C. For HLock01-B, we use larger apertures (2″–3″) on the lensed images A, C, and D, and then subtract the contribution of HLock01-R, which in any case is less than 5%. The lens

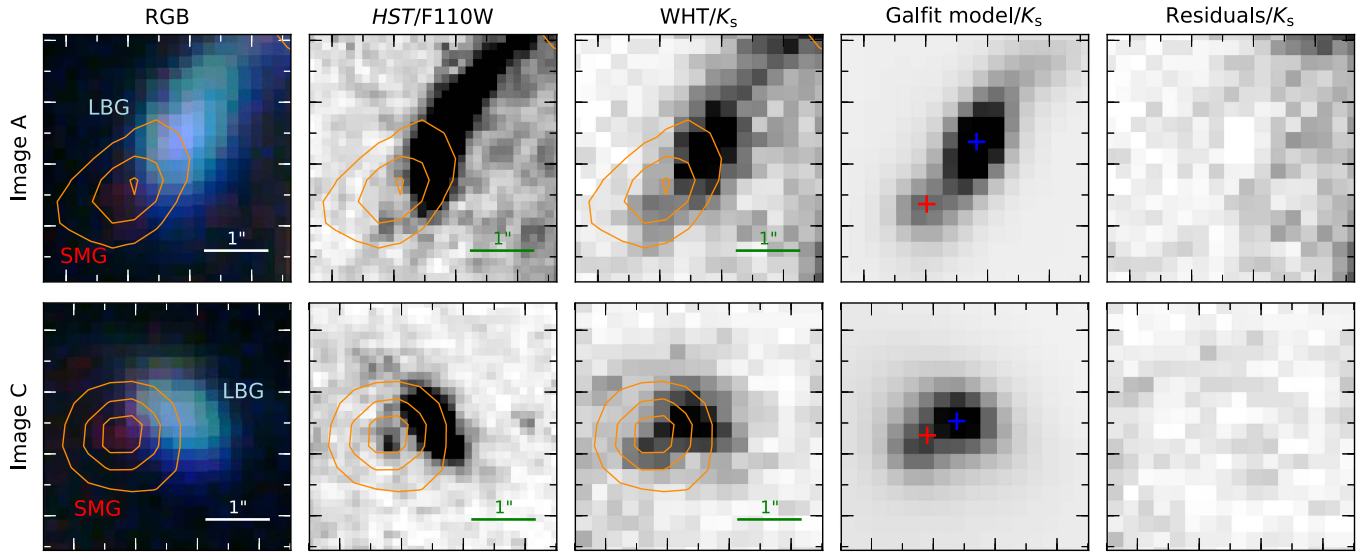

Figure 10. 4″ × 4″ cutouts of the lensed images A (upper panels) and C (lower panels) of HLock01. From left to right, we show a *g*, *I*, and K_s color image; high-resolution *HST*/WFC3 F110W; near-IR WHT/K_s; GALFIT model of the K_s data; and finally the resulting residuals after subtracting the K_s GALFIT model. 1.4 GHz VLA contours are in orange and correspond to the positions of two of the lensed images of the *Herschel* SMG. Blue and red crosses mark, respectively, the positions of the LBG and the SMG in our GALFIT model.

model was used again to add the light from the lensed image B.

Near-IR WHT/K_s photometry of the individual components (SMG and LBG of HLock01) was obtained after modeling the light distribution of each component in the lensed images A and C, using the two-dimensional fitting program GALFIT (Peng et al. 2002, 2010). We use Sérsic profiles centered at the centroids of the *HST*/F110W emission, allowing only one pixel freedom (≃0.″254). A nearby star was chosen as a point-spread function (PSF) model. Note that we only perform the fit in the lensed images A and C, the only ones that show detections of the faint, obscured counterparts of the SMG.[24] The lens model of Gavazzi et al. (2011) was used again to add the light from the lensed images B and C. Figure 10 shows our GALFIT model, as well as the resulting residuals after subtracting the K_s GALFIT model.

This field has been observed by the SWIRE survey (Lonsdale et al. 2003) in the cryogenic phase of *Spitzer* and to deeper levels in the two first bands of IRAC (3.6 and 4.5 μm) by the SERVS survey (Mauduit et al. 2012) in the post-cryogenic phase. In the *Spitzer* Enhanced Imaging Products (SEIP) catalog[25] of this area (based on the SWIRE data), the individual lensed images A and C are the only ones resolved and detected. However, their fluxes appear relatively large and inconsistent ($f_A/f_C \lesssim 1$) with the expected values from the individual magnifications provided by the lens model of Gavazzi et al. (2011; $f_A/f_C \simeq 1.7$). Given the limited spatial resolution of IRAC (≃2″), the cataloged fluxes of the lensed images A and C are likely contaminated by foreground light, mainly due to the G1, G4, and G6 lensing galaxies. To perform better photometry on HLock01, we use GALFIT to model the light distribution of both foreground and background components in the SERVS images. We use Sérsic profiles centered at the positions of the detected *HST*/F110W counterparts, and a nearby star was chosen as a PSF model. We then measure the flux density of our best-fit model of the lensed images A and C, and use the lens model to add the expected light from the other lensed images to obtain the total observed flux. Modeling the light distribution using GALFIT to separate the fluxes from the SMG and the LBG does not help and will introduce significant uncertainties in their measurements, since the spatial separation of the SMG and the LBG in the lensed images A and C is substantially lower (≃0.″9) than the intrinsic PSF in IRAC data (≃2″ FWHM). Finally, in the 8.0 μm IRAC band, the foreground light contamination appears to be much lower than in the other IRAC bands; thus we use the 3.″8 aperture photometry for the lensed images A and C provided in the SEIP catalog, with the appropriate aperture corrections. Again, we use the lens model to add the expected light of the lensed images B and D.

[24] This can be explained through the lensed images A and C being less affected by foreground contamination, and their lensing magnifications are higher than the ones of images B and D (see Gavazzi et al. 2011).

[25] http://irsa.ipac.caltech.edu/data/SPITZER/Enhanced/SEIP/

Appendix C
Lens Modeling

We use the ≃0.″2 FWHM *HST*/F110W image data to update the lens model already described in Gavazzi et al. (2011). The procedure is identical and uses the dedicated code SL_FIT (for more details, see also Gavazzi et al. 2007, 2008, 2011, 2012). We fit model parameters of simple analytical lensing potentials and model background galaxies as simple elliptical Sérsic profiles. The lensing potential is primarily constrained by the *HST* data, with the highest resolution and S/N. The mass distribution is then held fixed in order to fit for the parameters defining the light distribution in the other channels. We assume the deflector to be made of an isothermal elliptical mass distribution centered on the galaxy G1, and we also include the perturbing galaxies G2, G3, and G4 as point masses centered on the substructure light emission. We allow for the presence of a core radius that softens the inner mass distribution in each case. Unlike in Gavazzi et al. (2011), we do not place masses at G5 and G6, since they have a negligible impact on the mass model and their masses are essentially unconstrained. G1, being by far the most massive galaxy in the vicinity, is assumed to be at the center of the group-scale total mass distribution. The collective effect of a few possible perturbing galaxies 10″–20″ south of G1 may induce some external shear, which will contribute to the quadrupole of the mass distribution, but having too few constraints spanning too small a radial range around G1, we assume that the ellipticity of

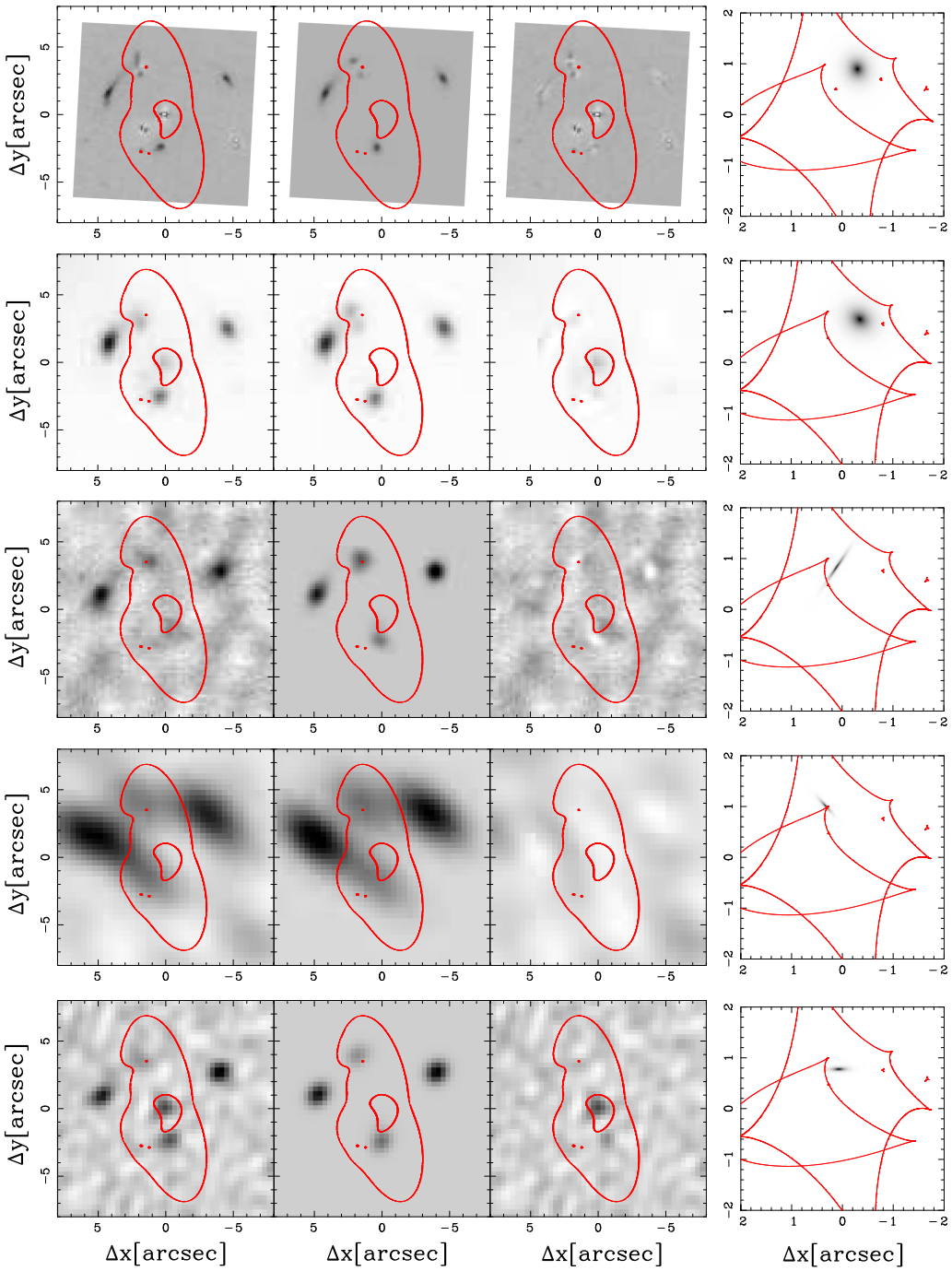

Figure 11. Lens inversion results in several bands. Top to bottom: *HST* F110W; GTC g band; 880 μm SMA; PdBI CO ($J = 5 \rightarrow 4$); and VLA 1.4 GHz observations. From left to right: input image (foreground deflectors are preliminarily subtracted off for *HST*); reconstructed image plane model; residual of input—reconstructed image; and finally the source plane reconstruction. All the images are centered on the lensing galaxy G1 ($\alpha = +10{:}57{:}50.959$, $\delta = +57{:}30{:}25.66$, J2000) and oriented such that north is up and east is to the left. At long wavelengths, the limited spatial resolution induces large fluctuations in the shown reconstructed maximum a posteriori sources (right panels), which can get very elongated (see Figure 7 for a comparison of more realistic posterior mean sources).

the mass distribution centered on G1 will absorb the total quadrupole. Higher order effects (like $m = 1$ or $m = 3$ multipoles) would also be hard to constrain with the current data.

The lensed features exhibiting a cross-like (or barely fold-like) configuration requires a source relatively close to the optical axis, and thus, relatively far for a widely opened main astroid caustic. We do not expect much magnification nor huge spatial variations of the magnification over the extent of the source. This contrasts with a cusp configuration (see, e.g., the cluster MS 0451.6-0305 in MacKenzie et al. 2014).

Modeling the *HST* F110W data first, we assume the background source is made of one single elliptical exponential profile for which we adjust source plane position, ellipticity, orientation, effective radius, and flux. Before fitting the lensed light emission, we performed a fit to the foreground light emission (i.e., G1–G5) in order to subtract it off. The result is shown in the top row panels of Figure 11. The formal uncertainty on the recovered Einstein radius (i.e., lens amplitude) is unrealistically small (∼0.2% relative), given the high S/N of the widely extended lensed images. However, large-scale structure mass

fluctuations along the line of sight, as well as unaccounted for substructures in the lensing mass distribution, should place a lower limit of order 1%–2% on the accuracy to which the Einstein radius can be measured. By artificially increasing the pixel rms errors in the F110W imaging data by a factor of 10, we are able to mimic this additional source of noise. As a result, we achieve a 1% accuracy on the recovered Einstein radius as $4\farcs08 \pm 0\farcs05$, consistent with the previous model of Gavazzi et al. (2011). The core radius is found to be $1\farcs1 \pm 0\farcs1$, and the mass distribution is very elongated, with an axis ratio $b/a = 0.38 \pm 0.03$. The mass of perturbing galaxies is poorly constrained: $M_{G2} = (6.0^{+5.1}_{-4.3}) \times 10^{10}\,M_{\odot}$, $M_{G3} \leqslant 4.4 \times 10^{10}\,M_{\odot}$, except the case of G4, which induces a splitting of one of the multiple images (B1–B2), yielding $M_{G4} = (9.1^{+6.0}_{-2.6}) \times 10^{10}\,M_{\odot}$. We find a total magnification $\mu = 8.5 \pm 0.5$ in the *HST* F110W band. The formal errors on magnification do not account for the mass-sheet degeneracy (related to a strong assumption about the mass density slope), which is responsible for the differences with the magnification we reported in Gavazzi et al. (2011). Channel-to-channel differential magnifications are, on the other hand, more robust and do not depend on the assumed mass distribution. From the best-fit mass model inferred from *HST* F110W data, we extract for the position, ellipticity, size, and flux of an exponential disk in the GTC, VLA, PdBI CO ($J = 5 \rightarrow 4$), and SMA continuum data. The output of the modeling in all the channels is shown in Figure 11. From top to bottom, each row represents the results of *HST* F110W, GTC g band, 880 μm SMA, PdBI CO ($J = 5 \rightarrow 4$), and VLA 1.4 GHz observations. The overall aspect does not change much with respect to the model of Gavazzi et al. (2011). The geometry of the source at long wavelengths is poorly determined, and the elongated shape of the best-fit sources in the lower panels is not significant.

ORCID iDs

Rui Marques-Chaves https://orcid.org/0000-0001-8442-1846
Dominik Riechers https://orcid.org/0000-0001-9585-1462
Antonio Cabrera-Lavers https://orcid.org/0000-0002-9153-8724
David L. Clements https://orcid.org/0000-0002-9548-5033
Duncan Farrah https://orcid.org/0000-0003-1748-2010
Rob J. Ivison https://orcid.org/0000-0001-5118-1313
Hooshang Nayyeri https://orcid.org/0000-0001-8242-9983
Seb Oliver https://orcid.org/0000-0001-7862-1032
Alain Omont https://orcid.org/0000-0002-4721-3922
Douglas Scott https://orcid.org/0000-0002-6878-9840
Julie Wardlow https://orcid.org/0000-0003-2376-8971

References

Alaghband-Zadeh, S., Chapman, S. C., Swinbank, A. M., et al. 2012, MNRAS, 424, 2232
Allam, S. S., Tucker, D. L., Lin, H., et al. 2007, ApJL, 662, L51
Álvarez-Márquez, J., Burgarella, D., Heinis, S., et al. 2016, A&A, 587, A122
Bayliss, M. B., Hennawi, J. F., Gladders, M. D., et al. 2011, ApJS, 193, 8
Belokurov, V., Evans, N. W., Moiseev, A., et al. 2007, ApJL, 671, L9
Berta, S., Lutz, D., Santini, P., et al. 2013, A&A, 551, A100
Bertin, E. 2006, in ASP Conf. Ser. 351, Astronomical Data Analysis Software and Systems XV, ed. C. Gabriel et al. (San Francisco, CA: ASP), 112
Bertin, E. 2010, SWarp: Resampling and Co-adding FITS Images Together, Astrophysics Source Code Library, ascl:1010.068
Bian, F., Fan, X., Jiang, L., et al. 2012, ApJ, 757, 139
Blain, A. W., Smail, I., Ivison, R. J., Kneib, J.-P., & Frayer, D. T. 2002, PhR, 369, 111
Bouché, N., Murphy, M. T., Kacprzak, G. G., et al. 2013, Sci, 341, 50
Bournaud, F., Perret, V., Renaud, F., et al. 2014, ApJ, 780, 57
Bridge, C. R., Appleton, P. N., Conselice, C. J., et al. 2007, ApJ, 659, 931
Bruzual, G., & Charlot, S. 2003, MNRAS, 344, 1000
Bussmann, R. S., Pérez-Fournon, I., Amber, S., et al. 2013, ApJ, 779, 25
Cabanac, R. A., Valls-Gabaud, D., & Lidman, C. 2008, MNRAS, 386, 2065
Calanog, J. A., Fu, H., Cooray, A., et al. 2014, ApJ, 797, 138
Calzetti, D., Armus, L., Bohlin, R. C., et al. 2000, ApJ, 533, 682
Capak, P., Carilli, C. L., Lee, N., et al. 2008, ApJL, 681, L53
Capak, P. L., Riechers, D., Scoville, N. Z., et al. 2011, Natur, 470, 233
Carilli, C. L., Daddi, E., Riechers, D., et al. 2010, ApJ, 714, 1407
Casey, C. M., Cooray, A., Capak, P., et al. 2015, ApJL, 808, L33
Casey, C. M., Cooray, A., Killi, M., et al. 2017, ApJ, 840, 101
Casey, C. M., Narayanan, D., & Cooray, A. 2014, PhR, 541, 45
Chabrier, G. 2003, ApJL, 586, L133
Chapman, S. C., Blain, A. W., Smail, I., & Ivison, R. J. 2005, ApJ, 622, 772
Chapman, S. C., Smail, I., Blain, A. W., & Ivison, R. J. 2004, ApJ, 614, 671
Charlot, S., & Fall, S. M. 2000, ApJ, 539, 718
Coil, A. L., Weiner, B. J., Holz, D. E., et al. 2011, ApJ, 743, 46
Conley, A., Cooray, A., Vieira, J. D., et al. 2011, ApJL, 732, L35
Coppin, K. E. K., Swinbank, A. M., Neri, R., et al. 2007, ApJ, 665, 936
da Cunha, E., Charlot, S., & Elbaz, D. 2008, MNRAS, 388, 1595
da Cunha, E., Walter, F., Smail, I. R., et al. 2015, ApJ, 806, 110
Daddi, E., Bournaud, F., Walter, F., et al. 2010, ApJ, 713, 686
Daddi, E., Dannerbauer, H., Stern, D., et al. 2009, ApJ, 694, 1517
Dahle, H., Aghanim, N., Guennou, L., et al. 2016, A&A, 590, L4
Danielson, A. L. R., Swinbank, A. M., Smail, I., et al. 2017, ApJ, 840, 78
Dannerbauer, H., Kurk, J. D., De Breuck, C., et al. 2014, A&A, 570, A55
Davé, R., Oppenheimer, B. D., & Finlator, K. 2011, MNRAS, 415, 11
Dekel, A., Birnboim, Y., Engel, G., et al. 2009, Natur, 457, 451
Delvecchio, I., Smolčić, V., Zamorani, G., et al. 2017, A&A, 602, A3
Dessauges-Zavadsky, M., D'Odorico, S., Schaerer, D., et al. 2010, A&A, 510, A26
Dowell, C. D., Conley, A., Glenn, J., et al. 2014, ApJ, 780, 75
Emonts, B. H. C., Lehnert, M. D., Villar-Martín, M., et al. 2016, Sci, 354, 1128
Erb, D. K., Pettini, M., Shapley, A. E., et al. 2010, ApJ, 719, 1168
Farrah, D., Rowan-Robinson, M., Oliver, S., et al. 2001, MNRAS, 326, 1333
Farrah, D., Verma, A., Oliver, S., Rowan-Robinson, M., & McMahon, R. 2002, MNRAS, 329, 605
Fu, H., Cooray, A., Feruglio, C., et al. 2013, Natur, 498, 338
Fu, H., Hennawi, J. F., Prochaska, J. X., et al. 2016, ApJ, 832, 52
Gavazzi, R., Cooray, A., Conley, A., et al. 2011, ApJ, 738, 125
Gavazzi, R., Treu, T., Koopmans, L. V. E., et al. 2008, ApJ, 677, 1046
Gavazzi, R., Treu, T., Marshall, P. J., Brault, F., & Ruff, A. 2012, ApJ, 761, 170
Gavazzi, R., Treu, T., Rhodes, J. D., et al. 2007, ApJ, 667, 176
González, J. E., Lacey, C. G., Baugh, C. M., & Frenk, C. S. 2011, MNRAS, 413, 749
Greve, T. R., Bertoldi, F., Smail, I., et al. 2005, MNRAS, 359, 1165
Gwyn, S. D. J. 2008, PASP, 120, 212
Haan, S., Surace, J. A., Armus, L., et al. 2011, AJ, 141, 100
Hainline, L. J., Blain, A. W., Smail, I., et al. 2011, ApJ, 740, 96
Hayward, C. C., Narayanan, D., Kereš, D., et al. 2013, MNRAS, 428, 2529
Hayward, C. C., & Smith, D. J. B. 2015, MNRAS, 446, 1512
Hezaveh, Y. D., Marrone, D. P., & Holder, G. P. 2012, ApJ, 761, 20
Hopkins, P. F., Kereš, D., Oñorbe, J., et al. 2014, MNRAS, 445, 581
Ivison, R. J., Greve, T. R., Smail, I., et al. 2002, MNRAS, 337, 1
Ivison, R. J., Lewis, A. J. R., Weiss, A., et al. 2016, ApJ, 832, 78
Ivison, R. J., Magnelli, B., Ibar, E., et al. 2010a, A&A, 518, L31
Ivison, R. J., Morrison, G. E., Biggs, A. D., et al. 2008, MNRAS, 390, 1117
Ivison, R. J., Smail, I., Papadopoulos, P. P., et al. 2010b, MNRAS, 404, 198
Ivison, R. J., Swinbank, A. M., Smail, I., et al. 2013, ApJ, 772, 137
James, B. L., Pettini, M., Christensen, L., et al. 2014, MNRAS, 440, 1794
Jiménez-Andrade, E. F., Magnelli, B., Karim, A., et al. 2017, arXiv:1710.10181
Jones, G. C., Carilli, C. L., Shao, Y., et al. 2017, ApJ, 850, 180
Jones, T., Stark, D. P., & Ellis, R. S. 2012, ApJ, 751, 51
Kennicutt, R. C., Jr. 1998, ARA&A, 36, 189
Kereš, D., Katz, N., Weinberg, D. H., & Davé, R. 2005, MNRAS, 363, 2
Kimm, T., Slyz, A., Devriendt, J., & Pichon, C. 2011, MNRAS, 413, L51
Kriek, M., van Dokkum, P. G., Labbé, I., et al. 2009, ApJ, 700, 221

Law, D. R., Shapley, A. E., Steidel, C. C., et al. 2012, Natur, 487, 338
Le Fèvre, O., Cassata, P., Cucciati, O., et al. 2013, A&A, 559, A14
Leitherer, C., Leão, J. R. S., Heckman, T. M., et al. 2001, ApJ, 550, 724
Leitherer, C., Schaerer, D., Goldader, J. D., et al. 1999, ApJS, 123, 3
Lin, H., Buckley-Geer, E., Allam, S. S., et al. 2009, ApJ, 699, 1242
Lonsdale, C. J., Smith, H. E., Rowan-Robinson, M., et al. 2003, PASP, 115, 897
Lu, N., Zhao, Y., Díaz-Santos, T., et al. 2017, ApJL, 842, L16
Ma, B., Cooray, A., Calanog, J. A., et al. 2015, ApJ, 814, 17
MacKenzie, T. P., Scott, D., Smail, I., et al. 2014, MNRAS, 445, 201
Magdis, G. E., Elbaz, D., Hwang, H. S., et al. 2010a, ApJL, 720, L185
Magdis, G. E., Rigopoulou, D., Daddi, E., et al. 2017, A&A, 603, A93
Magdis, G. E., Rigopoulou, D., Hopwood, R., et al. 2014, ApJ, 796, 63
Magdis, G. E., Rigopoulou, D., Huang, J.-S., & Fazio, G. G. 2010b, MNRAS, 401, 1521
Magnelli, B., Lutz, D., Santini, P., et al. 2012, A&A, 539, A155
Mannucci, F., Cresci, G., Maiolino, R., et al. 2009, MNRAS, 398, 1915
Marques-Chaves, R., Pérez-Fournon, I., Shu, Y., et al. 2017, ApJL, 834, L18
Marrone, D. P., Spilker, J. S., Hayward, C. C., et al. 2018, Natur, 553, 51
Martin, C. L., Shapley, A. E., Coil, A. L., et al. 2012, ApJ, 760, 127
Mauduit, J.-C., Lacy, M., Farrah, D., et al. 2012, PASP, 124, 714
Messias, H., Dye, S., Nagar, N., et al. 2014, A&A, 568, A92
Michałowski, M. J., Dunlop, J. S., Cirasuolo, M., et al. 2012, A&A, 541, A85
Michałowski, M. J., Dunlop, J. S., Koprowski, M. P., et al. 2017, MNRAS, 469, 492
Miettinen, O., Delvecchio, I., Smolčić, V., et al. 2017, A&A, 606, A17
Narayanan, D., Turk, M., Feldmann, R., et al. 2015, Natur, 525, 496
Nayyeri, H., Cooray, A., Jullo, E., et al. 2017, ApJ, 844, 82
Olivares, V., Treister, E., Privon, G. C., et al. 2016, ApJ, 827, 57
Oliver, S. J., Bock, J., Altieri, B., et al. 2012, MNRAS, 424, 1614
Ono, Y., Ouchi, M., Harikane, Y., et al. 2017, PASJ, arXiv:1704.06004
Ono, Y., Ouchi, M., Shimasaku, K., et al. 2010, MNRAS, 402, 1580
Oteo, I., Ivison, R. J., Dunne, L., et al. 2016, ApJ, 827, 34
Oteo, I., Ivison, R. J., Dunne, L., et al. 2017a, arXiv:1709.02809
Oteo, I., Ivison, R. J., Negrello, M., et al. 2017b, arXiv:1709.04191
Oyaizu, H., Lima, M., Cunha, C. E., et al. 2008, ApJ, 674, 768
Patrício, V., Richard, J., Verhamme, A., et al. 2016, MNRAS, 456, 4191
Peng, C. Y., Ho, L. C., Impey, C. D., & Rix, H.-W. 2002, AJ, 124, 266
Peng, C. Y., Ho, L. C., Impey, C. D., & Rix, H.-W. 2010, AJ, 139, 2097
Pettini, M., Rix, S. A., Steidel, C. C., et al. 2002, ApJ, 569, 742
Pettini, M., Steidel, C. C., Adelberger, K. L., Dickinson, M., & Giavalisco, M. 2000, ApJ, 528, 96
Quider, A. M., Pettini, M., Shapley, A. E., & Steidel, C. C. 2009, MNRAS, 398, 1263
Quider, A. M., Shapley, A. E., Pettini, M., Steidel, C. C., & Stark, D. P. 2010, MNRAS, 402, 1467
Rawle, T. D., Egami, E., Bussmann, R. S., et al. 2014, ApJ, 783, 59
Reddy, N., Dickinson, M., Elbaz, D., et al. 2012, ApJ, 744, 154
Reddy, N. A., Erb, D. K., Pettini, M., Steidel, C. C., & Shapley, A. E. 2010, ApJ, 712, 1070
Reddy, N. A., & Steidel, C. C. 2009, ApJ, 692, 778
Reddy, N. A., Steidel, C. C., Fadda, D., et al. 2006, ApJ, 644, 792
Riechers, D. A., Bradford, C. M., Clements, D. L., et al. 2013, Natur, 496, 329
Riechers, D. A., Carilli, C. L., Capak, P. L., et al. 2014, ApJ, 796, 84
Riechers, D. A., Cooray, A., Omont, A., et al. 2011, ApJL, 733, L12
Riechers, D. A., Leung, T. K. D., Ivison, R. J., et al. 2017, ApJ, 850, 1
Rigby, J. R., Bayliss, M. B., Chisholm, J., et al. 2017a, arXiv:1710.07499
Rigby, J. R., Bayliss, M. B., Sharon, K., et al. 2017b, arXiv:1710.07294
Rigopoulou, D., Pereira-Santaella, M., Magdis, G. E., et al. 2018, MNRAS, 473, 20
Rix, S. A., Pettini, M., Leitherer, C., et al. 2004, ApJ, 615, 98
Rubin, K. H. R., Prochaska, J. X., Koo, D. C., & Phillips, A. C. 2012, ApJL, 747, L26
Salomé, P., Guélin, M., Downes, D., et al. 2012, A&A, 545, A57
Sato, T., Martin, C. L., Noeske, K. G., Koo, D. C., & Lotz, J. M. 2009, ApJ, 696, 214
Schinnerer, E., Groves, B., Sargent, M. T., et al. 2016, ApJ, 833, 112
Schneider, D. P., Hall, P. B., Richards, G. T., et al. 2005, AJ, 130, 367
Scott, K. S., Lupu, R. E., Aguirre, J. E., et al. 2011, ApJ, 733, 29
Serjeant, S. 2012, MNRAS, 424, 2429
Shapley, A. E., Steidel, C. C., Adelberger, K. L., et al. 2001, ApJ, 562, 95
Shapley, A. E., Steidel, C. C., Pettini, M., & Adelberger, K. L. 2003, ApJ, 588, 65
Siana, B., Smail, I., Swinbank, A. M., et al. 2009, ApJ, 698, 1273
Siana, B., Teplitz, H. I., Chary, R.-R., Colbert, J., & Frayer, D. T. 2008, ApJ, 689, 59
Smail, I., Chapman, S. C., Ivison, R. J., et al. 2003, MNRAS, 342, 1185
Smail, I., Swinbank, A. M., Richard, J., et al. 2007, ApJL, 654, L33
Sommariva, V., Mannucci, F., Cresci, G., et al. 2012, A&A, 539, A136
Spilker, J. S., Aravena, M., Marrone, D. P., et al. 2015, ApJ, 811, 124
Steidel, C. C., Adelberger, K. L., Shapley, A. E., et al. 2003, ApJ, 592, 728
Steidel, C. C., Erb, D. K., Shapley, A. E., et al. 2010, ApJ, 717, 289
Steidel, C. C., Giavalisco, M., Pettini, M., Dickinson, M., & Adelberger, K. L. 1996, ApJL, 462, L17
Steidel, C. C., Strom, A. L., Pettini, M., et al. 2016, ApJ, 826, 159
Swinbank, A. M., Chapman, S. C., Smail, I., et al. 2006, MNRAS, 371, 465
Swinbank, A. M., Lacey, C. G., Smail, I., et al. 2008, MNRAS, 391, 420
Swinbank, A. M., Smail, I., Bower, R. G., et al. 2005, MNRAS, 359, 401
Swinbank, A. M., Smail, I., Chapman, S. C., et al. 2004, ApJ, 617, 64
Tacconi, L. J., Genzel, R., Neri, R., et al. 2010, Natur, 463, 781
Tacconi, L. J., Genzel, R., Smail, I., et al. 2008, ApJ, 680, 246
Toft, S., Zabl, J., Richard, J., et al. 2017, Natur, 546, 510
Trump, J. R., Hall, P. B., Reichard, T. A., et al. 2006, ApJS, 165, 1
Walter, F., Decarli, R., Carilli, C., et al. 2012, Natur, 486, 233
Wang, L., Dutton, A. A., Stinson, G. S., et al. 2015, MNRAS, 454, 83
Wardlow, J. L., Cooray, A., De Bernardis, F., et al. 2013, ApJ, 762, 59
Wiseman, P., Perley, D. A., Schady, P., et al. 2017, A&A, 607, A107
Wuyts, E., Barrientos, L. F., Gladders, M. D., et al. 2010, ApJ, 724, 1182
Wuyts, E., Rigby, J. R., Gladders, M. D., & Sharon, K. 2014, ApJ, 781, 61
Yee, H. K. C., Ellingson, E., Bechtold, J., Carlberg, R. G., & Cuillandre, J.-C. 1996, AJ, 111, 1783
York, D. G., Adelman, J., Anderson, J. E., Jr., et al. 2000, AJ, 120, 1579